

1 **NF1 regulates mesenchymal glioblastoma plasticity and aggressiveness**
2 **through the AP-1 transcription factor FOSL1**

3
4 Carolina Marques¹, Thomas Unterkircher², Paula Kroon¹, Annalisa Izzo², Gaetano
5 Gargiulo³, Eva Kling², Oliver Schnell², Sven Nelander⁴, Erwin F. Wagner^{5,6,7}, Latifa
6 Bakiri^{5,7}, Maria Stella Carro^{2*} and Massimo Squatrito^{1*}

7
8 ¹Seve Ballesteros Foundation Brain Tumor Group, Spanish National Cancer Research
9 Centre, CNIO, 28029 Madrid, Spain.

10 ²Department of Neurosurgery, Faculty of Medicine Freiburg, D-79106 Freiburg,
11 Germany.

12 ³Max-Delbrück-Center for Molecular Medicine (MDC), Robert-Rössle-Str. 10, 13092
13 Berlin, Germany.

14 ⁴Dept of Immunology, Genetics and Pathology and Science for Life Laboratory,
15 Uppsala University, Rudbecklaboratoriet, SE-751 85 Uppsala, Sweden.

16 ⁵Genes, Development, and Disease Group, Spanish National Cancer Research Centre,
17 CNIO, 28029 Madrid, Spain.

18 ⁶Dermatology Department, Medical University of Vienna, A-1090 Vienna, Austria.

19 ⁷Laboratory Medicine Department, Medical University of Vienna, A-1090 Vienna,
20 Austria.

21
22 * Correspondence: maria.carro@uniklinik-freiburg.de; msquatrito@cnio.es

23
24 Lead contact: Massimo Squatrito

25 **Summary**

26 The molecular basis underlying Glioblastoma (GBM) heterogeneity and plasticity are not
27 fully understood. Using transcriptomic data of patient-derived brain tumor stem cell lines
28 (BTSCs), classified based on GBM-intrinsic signatures, we identify the AP-1
29 transcription factor *FOSL1* as a master regulator of the mesenchymal (MES) subtype. We
30 provide a mechanistic basis to the role of the Neurofibromatosis type 1 gene (*NF1*), a
31 negative regulator of the RAS/MAPK pathway, in GBM mesenchymal transformation
32 through the modulation of *FOSL1* expression. Depletion of *FOSL1* in NF1-mutant human
33 BTSCs and Kras-mutant mouse neural stem cells results in loss of the mesenchymal gene
34 signature, reduction in stem cell properties and *in vivo* tumorigenic potential. Our data
35 demonstrate that *FOSL1* controls GBM plasticity and aggressiveness in response to *NF1*
36 alterations.

37

38 **Keywords**

39 GBM, Mesenchymal, NF1, FOSL1, FRA-1, master regulator

40

41 **Significance**

42 Glioblastoma (GBM) is a very heterogeneous disease for which multiple transcriptional
43 subtypes have been described. Among these subtypes, the Mesenchymal (MES) GBMs
44 have the worst prognosis. Here we provide the first causal evidence linking
45 Neurofibromatosis type 1 gene (*NF1*) signalling and the acquisition of a MES gene
46 expression program through the regulation of the AP-1 transcription factor *FOSL1*. Using
47 patient expression datasets, combined with *in vitro* and *in vivo* gain- and loss- of function
48 mouse models, we show that *FOSL1* is an important modulator of GBM that is required
49 and sufficient for the activation of a MES program. Our work sheds light on the
50 mechanisms that control the tumorigenicity of the most aggressive adult brain tumor type.

51 **Introduction**

52 Glioblastoma (GBM), the most common and aggressive primary brain tumor in
53 adults, is characterized by high molecular and cellular inter- and intra-tumoral
54 heterogeneity. Large-scale sequencing approaches have evidenced how concurrent
55 perturbations of cell cycle regulators, growth and survival pathways, mediated by
56 RAS/MAPK and PI3K/AKT signaling, play a significant role in driving adult GBMs
57 (Brennan et al., 2013; The Cancer Genome Atlas Research Network, 2008; Verhaak et
58 al., 2010). Moreover, various studies have classified GBM in different subtypes, using
59 transcriptional profiling, being now the Proneural (PN), Classical (CL) and Mesenchymal
60 (MES) the most widely accepted (Phillips et al., 2006; Verhaak et al., 2010; Wang et al.,
61 2017).

62 Patients with the MES subtype tend to have worse survival rates compared to other
63 subtypes, both in the primary and recurrent tumor settings (Wang et al., 2017). The main
64 driver genetic alteration – Neurofibromatosis type 1 gene (*NFI*) copy number loss or
65 mutation – and important regulators of the MES subtype, such as STAT3, CEBPB and
66 TAZ, have been identified (Bhat et al., 2011; Carro et al., 2010; Verhaak et al., 2010).
67 Nevertheless, the mechanisms of regulation of MES GBMs are still not fully understood.
68 For example, whether the MES transcriptional signature is controlled through tumor cell-
69 intrinsic mechanisms or influenced by the tumor microenvironment (TME) is still an
70 unsolved question. In fact, the critical contribution of the TME adds another layer of
71 complexity to MES GBMs. Tumors from this subtype are highly infiltrated by non-
72 neoplastic cells, as compared to PN and CL subtypes (Wang et al., 2017). Additionally,
73 MES tumors express high levels of angiogenic markers and exhibit high levels of necrosis
74 (Cooper et al., 2012).

75 Even though each subtype is associated with specific genetic alterations, there is
76 a considerable plasticity among them: different subtypes co-exist in the same tumors and
77 shifts in subtypes can occur over time (Patel et al., 2014; Sottoriva et al., 2013). This
78 plasticity may be explained by acquisition of new genetic and epigenetic abnormalities,
79 by stem-like reprogramming or by clonal variation (Fedele et al., 2019). It is also not fully
80 understood whether the distinct subtypes evolve from a common glioma precursor
81 (Ozawa et al., 2014). For instance, PN tumors often switch phenotype to MES upon
82 recurrence, and treatment also increases the mesenchymal gene signature, suggesting that
83 MES transition, or epithelial to mesenchymal (EMT)-like, in GBM is associated with
84 tumor progression and therapy resistance (Bhat et al., 2013; Halliday et al., 2014; Phillips

85 et al., 2006). Yet, the frequency and relevance of this EMT-like phenomenon in glioma
86 progression remains unclear. EMT has also been associated with stemness in other
87 cancers (Mani et al., 2008; Tam and Weinberg, 2013; Ye et al., 2015). Glioma stem cells
88 (GSCs) share features with normal neural stem cells (NSCs) such as self-renewal and
89 ability to differentiate into distinct cellular lineages (astrocytes, oligodendrocytes and
90 neurons) but are thought to be the responsible for tumor relapse, given their ability to
91 repopulate tumors and their resistance to treatment (Bao et al., 2006; Chen et al., 2012).

92 *FOSL1*, that encodes FRA-1, is an AP-1 transcription factor with prognostic value
93 in different epithelial tumors, where its overexpression correlates with tumor progression
94 or worse patient survival (Chiappetta et al., 2007; Gao et al., 2017; Usui et al., 2012;
95 Vallejo et al., 2017; Wu et al., 2015; Xu et al., 2017). Moreover, the role of *FOSL1* in
96 EMT has been documented in breast and colorectal cancers (Andreolas et al., 2008; Bakiri
97 et al., 2015; Diesch et al., 2014; Tam et al., 2013). In GBM, it has been shown that *FOSL1*
98 modulates *in vitro* glioma cell malignancy (Debinski and Gibo, 2005).

99 Here we report that *NFI* loss, by increasing RAS/MAPK activity, modulates
100 *FOSL1* expression which in turn plays a central function in the regulation of MES GBM.
101 Using a surrogate mouse model of MES GBM and patient-derived MES brain tumor stem
102 cells (BTSCs), we show that *FOSL1* is responsible for sustaining cell growth *in vitro* and
103 *in vivo*, and for the maintenance of stem-like properties. We propose that *FOSL1* is an
104 important regulator of GBM stemness, MES features and plasticity, controlling an EMT-
105 like process with therapeutically relevant implications.

106

107 **Results**

108 ***FOSL1* is a master regulator of the MES subtype**

109 To study the tumor cell-intrinsic signaling pathways that modulate the GBM
110 expression subtypes we assembled a collection of transcriptomic data (both expression
111 arrays and RNA-sequencing) of 115 samples derived from 87 independent BTSC lines:
112 24 newly generated at Freiburg Medical Center, 44 from GSE119834 (Mack et al., 2019),
113 10 from GSE67089 (Mao et al., 2013) and 9 from GSE8049 (Günther et al., 2008).
114 Samples were then classified according to the previously reported 50-gene glioma-
115 intrinsic transcriptional subtype signatures and the single sample gene set enrichment
116 analysis (ssGSEA)-based equivalent distribution resampling classification strategy
117 (Wang et al., 2017). Overall, 39% of the samples were identified as CL, 41% as MES and
118 20% as PN (Table S1). Principal component analysis showed a large overlap of the

119 transcription profile among CL and PN BTSCs while most of the MES BTSCs appeared
120 as a separate group (Figure 1A). Differential gene expression analysis comparing MES
121 versus Non-MES (PN and CL) BTSCs confirmed a clear separation among the two
122 groups, with the exception of a small number of cell lines that showed a mixed expression
123 profile (Figure 1B and Table S2).

124 To reveal the signaling pathways underlying the differences among MES versus
125 Non-MES BTSCs we then applied a network-based approach based on ARACNe
126 (Algorithm for the Reconstruction of Accurate Cellular Networks) (Basso et al., 2005;
127 Carro et al., 2010), which identifies a list of transcription factors (TFs) with their predicted
128 targets, defined as regulons. The regulon for each TF is constituted by all the genes whose
129 expression data exhibit significant mutual information with that of a given TF and are
130 thus expected to be regulated by that TF (Castro et al., 2016; Fletcher et al., 2013).
131 Enrichment of a relevant gene signature in each of the regulons can point to the TFs acting
132 as master regulators (MRs) of the response or phenotype (Carro et al., 2010; Fletcher et
133 al., 2013). Master regulator analysis (MRA), identified a series of TFs, among which
134 *FOSL1*, *SOX11*, *OLIG2*, *CTCF* and *IRF1* were the top 5 most statistically significant
135 (Benjamini-Hochberg $P < 0.0001$) (Table S3 and Figure 1C). *FOSL1* and *IRF1* were
136 significantly upregulated in the MES BTSCs, while *SOX11*, *OLIG2*, *CTCF* were
137 upregulated in the Non-MES BTSCs (Figure S1A and 1D). Gene set enrichment analysis
138 (GSEA) evidenced how the regulons for the top 5 TFs are enriched for genes that are
139 differentially expressed among the two classes (MES and Non-MES) with *FOSL1* having
140 the highest enrichment score (Figure 1C and Figure S1B).

141 We then analyzed the TCGA pan-glioma dataset (Ceccarelli et al., 2016) and
142 observed that *FOSL1* expression is elevated in the IDH-wt glioma molecular subtype
143 (Figure 1E and Table S4) and that high expression levels are associated with worse
144 prognosis in IDH-wt GBM (Figure 1F), thus suggesting that *FOSL1* could represent not
145 only a master regulator of the glioma-intrinsic MES signature, but also a putative key
146 player in MES GBM pathogenesis.

147

148 ***NFI* modulates the MES signature and *FOSL1* expression**

149 *NFI* alterations and activation of the RAS/MAPK signaling have been previously
150 associated with the MES GBM subtype (Brennan et al., 2013; Verhaak et al., 2010; Wang
151 et al., 2016; Wang et al., 2017). However, whether *NFI* plays a functional role in the
152 regulation of the MES gene signature (MGS) still remains to be established.

153 We initially grouped, according to the previously described subtype-specific gene
154 signatures, a subset of IDH-wt GBM samples of the TCGA dataset for which RNA-seq
155 data were available ($n = 152$) (see methods for details). By analyzing the frequency of
156 *NF1* alterations (either point mutations or biallelic gene loss) in the different subtypes
157 (Figure 2A), we confirmed a significant enrichment of *NF1* alterations in MES versus
158 Non-MES tumors (Fisher's Exact test P value = 0.03) (Figure 2B). Importantly, we
159 detected higher level of *FOSL1* mRNA in the cohort of patient tumors with *NF1*
160 alterations, both low-grade gliomas (LGGs) and GBMs (Figures 2C and Table S4), with
161 the NF1-altered MES GBMs showing the highest expression levels (Figures 2D and Table
162 S4).

163 To test whether *NF1* signaling is directly involved in the regulation of *FOSL1* and
164 the MES subtype, we manipulated NF1 expression in patient derived tumorspheres of
165 either the MES or PN subtype (Figure S3A-B). To recapitulate the activity of the full-
166 length NF1 protein we transduced the cells with the NF1 GTPase-activating domain
167 (NF1-GRD), spanning the whole predicted Ras GTPase-activating (GAP) domain
168 (McCormick, 1990). NF1-GRD expression in the MES cell line BTSC 233 led to
169 inhibition of RAS activity as confirmed by analysis of pERK expression upon EGF or
170 serum stimulation (Figure S2A-B) as well as by RAS pull down assay (Figure S2C).
171 Furthermore, analysis of a RAS-induced oncogenic signature expression by GSEA
172 showed a strong reduction in NF1-GRD expressing cells (NES = -1.7; FDR q-value <
173 0.001) (Figure S2D). Most importantly, NF1-GRD expression led to a significant
174 reduction of the MGSs (Wang signature: NES = -1.3; FDR q-value = 0.05; Phillips
175 signature: NES = -1.7; FDR q-value < 0.001) (Figure 2E, left panels). On the contrary,
176 Proneural gene signatures (PNGSs) were upregulated (Wang signature: NES = 1.2; FDR
177 q-value = 0.12; Phillips signature: NES = 1.3; FDR q-value = 0.1) (Figure 2E, right
178 panels). Western blot analysis also revealed a significant decrease of CHI3L1 expression,
179 a well characterized mesenchymal marker, upon NF1-GRD overexpression (Figure 2F).

180 Mesenchymal glioblastoma cells are able to differentiate into osteocytes, a feature
181 they share with mesenchymal stem cells (Ricci-Vitiani et al., 2008; Tso et al., 2006).
182 Consistent with the loss of the MGS, the ability to differentiate into osteocytes was lost
183 in the BTSC 233 MES cells transduced with the NF1-GRD, as documented by Alizarin
184 Red staining (Figure 2G).

185 To further confirm whether *NF1* deletion could be sufficient to induce changes in
186 the MGS, we then knocked down *NF1* in the NF1-expressing PN cell line BTSC 3021

187 (Figure 2H) and performed microarray gene expression analysis followed by GSEA. Both
188 Wang and Phillips MGSs were enriched upon NF1 silencing (Wang: NES = 1.61; FDR
189 q-value = 0.005; Phillips: NES = 1.9; FDR q-value < 0.001) (Figure 2I). The PNGSs
190 instead were not significantly lost (data not shown).

191 Taken together, our data indicate that NF1 modulation is able to alter the MGS
192 expression in GBM. NF1-led gene expression changes might be driven by an effect on
193 MGS master regulators. Alternatively, other TFs might be involved. We therefore
194 analyzed the expression of *FOSL1* and other previously described mesenchymal TFs
195 (Bhat et al., 2011; Carro et al., 2010) upon NF1-GRD overexpression or *NF1* loss in two
196 independent MES (BTSC 233 and BTSC 232) or PN (BTSC 3021 and BTSC 3047) cell
197 lines. Interestingly, only *CEBPB* and *FOSL1* were consistently downregulated upon NF1-
198 GRD expression (Figure 2J and S3C) and upregulated following *NF1* knockdown
199 (Figures 2K and S3D). Moreover, a *FOSL1* targets signature was enriched in the *NF1*
200 altered versus *NF1* wt GBM samples of the TCGA dataset as well as in the BTSC 3021
201 sh*NF1* versus shCtrl (*NF1* altered: NES = 1.38; FDR q-value = 0.16; sh*NF1*: NES = 1.9;
202 FDR q-value < 0.001) (Figure S3E, top and middle panels). Conversely, *FOSL1* targets
203 were downregulated upon NF1-GRD (NF1-GRD: NES = -1.38; FDR q-value = 0.037)
204 (Figure S3E, bottom panel). These data were further confirmed by the analysis of the
205 expression of some *FOSL1* targets (*ITGA3*, *PLAU*, *ITGA5*, *TNC* and *SERPINE1*): we
206 observed that *ITGA3* and *SERPINE1* were consistently either downregulated upon NF1-
207 GRD overexpression (Figure S3F, NF1-GRD in BTSC 233 and BTSC 232) or
208 upregulated upon *NF1* knockdown (Figure S3G, sh*NF1* in BTSC 3021 and BTSC 3047).

209 Overall these evidences suggest that *NF1* is directly involved in the regulation of
210 the MGS, possibly through the modulation of *FOSL1* expression.

211

212 ***Fosl1* deletion induces a shift from a MES to a PN gene signature**

213 To further explore the *NF1-FOSL1* axis in MES GBM we used a combination of
214 the RCAS-Tva system with the CRISPR/Cas9 technology, recently developed in our
215 laboratory (Oldrini et al., 2018) to induce *Nf1* loss or *Kras* mutation. Mouse neural stem
216 cells (NSCs) from *hGFAP-Tva*; *hGFAP-Cre*; *Trp53^{lox}*; *ROSA26-LSL-Cas9* pups were
217 isolated and infected with viruses produced by DF1 packaging cells transduced with
218 RCAS vectors targeting the expression of *Nf1* through shRNA and sgRNA (sh*Nf1* and
219 sg*Nf1*) or overexpressing a mutant form of *Kras* (*Kras^{G12V}*). Loss of NF1 expression was
220 confirmed by western blot and FRA-1 was upregulated in the two models of *Nf1* loss

221 compared to parental cells, and further upregulated in cells infected with *Kras*^{G12V} (Figure
222 3A). Consistent with activation of the Ras signaling, as result of both *Nf1* loss and *Kras*
223 mutation, the MEK/ERK pathway was more active in infected cells compared to parental
224 cells (Figure 3A). Higher levels of activation of the MEK/ERK pathway were associated
225 with the induction of mesenchymal genes such as *Plau*, *Plaur*, *Timp1* and *Cd44* (Figure
226 3B). These data indicated that *Kras*^{G12V}-transduced cells are a suitable model to
227 functionally study the role of *Fos11* in MES GBM.

228 Taking advantage of the Cas9 expression in the generated cell p53-null *Kras*^{G12V}
229 NSCs model, *Fos11* expression was knocked out through sgRNAs. Efficient
230 downregulation of FRA-1 was achieved with 2 different sgRNAs (Figure 3C). Cells
231 transduced with sg*Fos11*_1 and sg*Fos11*_3 were then subjected to further studies.

232 As suggested by the data presented here on the human BTSCs datasets (Figures
233 1C-D and 2K), *FOSL1* appears to be a key regulator the MES subtype. Consistently,
234 RNA-seq analysis followed by GSEA of p53-null *Kras*^{G12V} sg*Fos11*_1 versus sgCtrl
235 revealed a significant loss of Wang and Phillips MGSs (Wang: NES = -1.85; FDR q-value
236 < 0.001; Phillips: NES = -1.91; FDR q-value < 0.001) (Figure 3D, left panels).
237 Oppositely, Wang and Phillips PNGSs were increased in sg*Fos11*_1 cells (Wang: NES =
238 1.42; FDR q-value = 0.029; Phillips: NES = 2.10; FDR q-value < 0.001) (Figure 3D, right
239 panels). These findings were validated by qRT-PCR with a significant decrease in
240 expression of a panel of MES genes (*Plau*, *Itga7*, *Timp1*, *Plaur*, *Fn1*, *Cyr61*, *Actn1*,
241 *SI00a4*, *Vim*, *Cd44*) (Figure 3E) and increased expression of PN genes (*Olig2*, *Ncam1*,
242 *Bcan*, *Lgr5*) in the *Fos11* knock-out (KO) *Kras*^{G12V} NSCs (Figure 3F).

243

244 ***Fos11* deletion reduces stemness and tumor growth**

245 Ras activating mutations have been widely used to study gliomagenesis, in
246 combination with other alterations as Akt mutation (Holland et al., 2000), loss of
247 Ink4a/Arf (Uhrbom et al., 2002) or p53 (Friedmann-Morvinski et al., 2012; Koschmann
248 et al., 2016; Muñoz et al., 2013). Thus, we then explored the possibility that *Fos11* could
249 modulate the tumorigenic potential of the p53-null *Kras* mutant cells.

250 Cell viability was significantly decreased in *Fos11* KO cell lines, as compared to
251 sgCtrl (Figure 4A). Concomitantly, we observed a significant decreased percentage of
252 cells in S-phase (mean values: sgCtrl = 42.6%; sg*Fos11*_1 = 21.6%, P ≤ 0.001; sg*Fos11*_3
253 = 20.4%, P = 0.003) and an increase in percentage of cells in G2/M (mean values: sgCtrl
254 = 11.7%, sg*Fos11*_1 = 28.4%, P ≤ 0.001; sg*Fos11*_3 = 23.4%, P = 0.012) (Figure 4B).

255 Another aspect that contributes to GBM aggressiveness is its heterogeneity,
256 attributable in part to the presence of glioma stem cells. By using limiting dilution assays,
257 we found that *Fosll* is required for the maintenance of stem cell capacity (Figure 4C).
258 Moreover, RNA-seq analysis showed that sg*Fosll*_1 cells downregulated the expression
259 of stem genes (*Elf4*, *Klf4*, *Itgb1*, *Nes*, *Sall4*, *L1cam*, *Melk*, *Cd44*, *Myc*, *Fut4*, *Cxcr4*,
260 *Prom1*) while upregulating the expression of lineage-specific genes: neuronal (*Map2*,
261 *Ncam1*, *Tubb3*, *Slc1a2*, *Rbfox3*, *Dcx*), astrocytic (*Aldh1l1*, *Gfap*, *S100b*, *Slc1a3*) and
262 oligodendrocytic (*Olig2*, *Sox10*, *Cnp*, *Mbp*, *Cspg4*) (Figure 4D). The different expression
263 of some of the stem/differentiation markers was confirmed also by immunofluorescence
264 analysis. While *Fosll* KO cells presented low expression of the stem cell marker CD44,
265 differentiation markers as GFAP and OLIG2 were significantly higher when compared to
266 sgCtrl cells (Figure 4E, Figure S4).

267 We then sought to test whether: i) p53-null *Kras*^{G12V} NSCs were tumorigenic and
268 ii) *Fosll* played any role in their tumorigenic potential. Intracranial injections of p53-null
269 *Kras*^{G12V} NSCs in *nu/nu* mice led to the development of high-grade tumors with a median
270 survival of 37 days in control cells (n=9). However, the sg*Fosll*_1 injected mice (n=6)
271 had a significant increase in median survival (54.5 days, Log-rank $P = 0.0263$) (Figure
272 4F). Consistent with what we detected *in vitro* (Figure 3D-F) we observed a switch from
273 a MGS to a PNGS in the tumors (Figure 4G-I). By western blot and immunohistochemical
274 analysis, we observed a reduction on expression of MES markers (VIM, CD44 and
275 S100A4) as compared to sgCtrl tumors (Figure 4G-H), while the PN marker OLIG2 was
276 only found expressed in sg*Fosll* tumors (Figure 4G). Similarly, when we compared
277 mRNA expression of a sgCtrl tumor with high FRA-1 expression (T4, Figure 4G) with
278 sg*Fosll* tumors with no detectable FRA-1 expression by western blot (T3 and T4, Figure
279 4G), we found downregulated expression of MES markers and upregulated expression of
280 PN markers in the sg*Fosll* tumors (Figure 4I-J).

281 Altogether, our data support the conclusion that, besides controlling cell
282 proliferation, *Fosll* plays a critical role in the maintenance of the stem cell properties and
283 tumorigenicity of p53-null *Kras* mutant NSCs.

284

285 ***Fosll* amplifies MES gene expression**

286 To further assess the role of *Fosll* as a key player in the control of the MGS, we
287 used a mouse model of inducible *Fosll* overexpression containing the alleles *Kras*^{LSL G12V};
288 *Trp53*^{lox}; *ROSA26*^{LSLrtTA-IRES-EGFP}; *Colla1*^{TetO-Fosll} (here referred as *Fosll*^{tetON}). Similar to

289 the loss-of-function approach here used, this allelic combination allows the expression of
290 *Kras*^{G12V} and deletion of *p53* after Cre recombination. Moreover, the expression of the
291 reverse tetracycline transactivator (rtTA) allows, upon induction with doxycycline (Dox),
292 the ectopic expression of *FosII* (Flag tagged), under the control of the *Coll1a1* locus and
293 a tetracycline-responsive element (TRE or Tet-O) (Belteki et al., 2005; Hasenfuss et al.,
294 2014).

295 NSCs derived from *FosII*^{WT} and *FosII*^{tetON} mice were infected *in vitro* with a
296 lentiviral vector expressing the Cre recombinase and efficient infection was confirmed by
297 fluorescence microscopy, as the cells expressing the rtTA should express GFP (data not
298 shown). FRA-1 overexpression, as well as Flag-tag expression was then tested by western
299 blot after 72h of Dox induction (Figure 5A). When *FosII*^{tetON} NSCs were analyzed by
300 qRT-PCR for the expression of MES/PN markers, a significant upregulation of most MES
301 genes and downregulation of PN genes was found in the cells overexpressing *FosII* upon
302 Dox induction (Figure 5B-C), the inverse image of our findings with *FosII* knock-out
303 cells.

304 In order to investigate if the MES phenotype induced with *FosII* overexpression
305 would have any effect *in vivo*, p53-null *Kras*^{G12V} *FosII*^{tetON} NSCs were intracranially
306 injected into syngeneic C57BL/6J wildtype mice. Injected mice were randomized and
307 subjected to Dox diet (food pellets and drinking water) or kept as controls with regular
308 food and drinking water with 1% sucrose. No differences in mice survival were observed
309 (Figure S5B). However, tumors developed from *FosII* overexpressing mice (+Dox) were
310 larger (Figure 5D), more infiltrative and with a more aggressive appearance than controls
311 (-Dox), that mostly grew as superficial tumor masses, even if both -Dox and +Dox
312 tumors seem to proliferate similarly (Figure S5C).

313 Tumorspheres were derived from -Dox and +Dox tumor-bearing mice and *FosII*
314 expression was manipulated *in vitro* through addition or withdrawal of Dox from the
315 culture medium. In the case of tumorspheres derived from a -Dox tumor, when Dox was
316 added for 19 days, high levels of FRA-1 expression were detected by western blot (Figure
317 5E). At the mRNA level, Dox treatment also greatly increased *FosII* expression, as well
318 as some of the MES genes (Figure 5F), while the expression of PN genes was
319 downregulated (Figure 5G). Conversely, when Dox was removed from +Dox derived
320 tumorspheres for 19 days, the expression of FRA-1 decreased (Figure 5H-I), along with
321 the expression of MES genes (Figure 5I), while PN genes were upregulated (Figure 5J).
322 These results confirm the essential role of *FosII* in the regulation of the MES gene

323 signature in p53-null *Kras*^{G12V} tumor cells and the plasticity between the PN and MES
324 subtypes.

325

326 ***FOSL1* controls growth, stemness and MES gene expression in patient-derived** 327 **tumor cells**

328 To prove the relevance of our findings in the context of human tumors, we
329 analyzed BTSC lines characterized as Non-MES (BTSC 268 and 409) or MES (BTSC
330 349 and 380) (Figure 1A). By western blot, we found that MES BTSC 380 did not express
331 NF1 while BTSC 349 showed a different pattern of NF1 expression compared to the Non-
332 MES lines BTSC 268 and 409 (intact NF1), that might be due to a *NF1* point mutation.
333 Consistent with the observed upon *NF1* silencing either in human BTSCs (Figure 2I) or
334 mouse NSCs (Figure 3A), both MES cell lines expressed high levels of FRA-1 and
335 activation of the MEK/ERK pathway (Figure 6A).

336 To study the role of *FOSL1* in the context of human BTSCs, its expression was
337 silenced in the MES BTSC 349, the cell line with higher FRA-1 expression, using a Dox
338 inducible shRNA. We confirmed by western blot FRA-1 downregulation after 3 days of
339 Dox treatment (Figure 6B). Similar to what was observed in the mouse cells, *FOSL1*
340 silencing in MES BTSC 349 resulted in reduced cell growth (Figure 6C) with a significant
341 reduction of the percentage of BrdU positive cells, compared to Dox-untreated cells
342 (Figure S6A). *FOSL1* silencing through Dox treatment also decreased stem cell sphere
343 forming capacity of MES BTSC 349 (Figure 6D). Moreover, *FOSL1* silencing resulted
344 also in the significant downregulation of the MES genes (Figure 6E), while no major
345 differences in the expression of PN genes was observed (Figure S6B).

346 Lastly, we tested whether FRA-1 modulates the MGS via direct target regulation.
347 To this end, we first identified high-confidence *FOSL1*/FRA-1 binding sites in chromatin
348 immunoprecipitation-seq (ChIP-seq) generated in non-mesenchymal cancer cells (see
349 methods) and then we determined the counts per million reads (CPM) of the enhancer
350 histone mark H3K27Ac in a set of MES and non-MES BTSCs (Mack et al., 2019).
351 Differential enrichment analysis by DeSeq2 revealed 9262 regions statistically significant
352 for H3K27Ac at *FOSL1*/FRA-1 binding sites in either MES or non-MES BTSCs (Figure
353 6F). Gene set enrichment analysis revealed that a significant fraction of H3K27Ac-
354 decorated *FOSL1*/FRA-1 binding sites was enriched in MES BTSCs and PCA further
355 revealed that H3K27Ac-decorated sites in MES BTSCs clustered closer to *FOSL1*/FRA-
356 1 direct binding to chromatin when compared to non-MES BTSCs (Figure 6G). Next, we

357 compared H3K27Ac distribution over *FOSL1*/FRA-1 binding sites to that of the Non-
358 MES master regulator OLIG2 (Figure 1C). This analysis showed that the 9262
359 *FOSL1*/FRA-1 binding sites are systematically decorated with H3K27Ac in MES BTSCs,
360 whereas only 3423 out of 9262 sites are acetylated to a similar extent in non-MES BTSCs.
361 Importantly, the inverse trend was observed for H3K27Ac at OLIG2 binding sites (Figure
362 6H). Validation in an independent MES BTSC line (BTSC 349) by ChIP-qPCR
363 confirmed FRA-1 binding at promoters of some MES genes including *PLAU*, *TNC*,
364 *ITGA5* and *CD44* (Figure 6J).

365 Altogether, our data support that *FOSL1*/FRA-1 regulates MES gene expression
366 and aggressiveness in human gliomas via direct transcriptional regulation, downstream
367 of NF1.

368

369 **Discussion**

370 The most broadly accepted transcriptional classification of GBM was originally
371 based on gene expression profiles of bulk tumors (Verhaak et al., 2010), which did not
372 discriminate the contribution of tumor cells and TME to the transcriptional signatures. It
373 is now becoming evident that both cell-intrinsic and extrinsic cues can contribute to the
374 specification of the MES subtype (Bhat et al., 2013; Neftel et al., 2019; Wang et al., 2017).
375 Bhat and colleagues had shown that while some of the MES GBMs maintained the
376 mesenchymal characteristics when expanded *in vitro* as BTSCs, some others lost the
377 MGS after few passages while exhibiting a higher PNGS (Bhat et al., 2013). These data,
378 together with the evidence that xenografts into immunocompromised mice of BTSCs
379 derived from MES GBMs were also unable to fully restore the MES phenotype, suggested
380 that the presence of an intact TME potentially contributed to the maintenance of a MGS,
381 either by directly influencing a cell-intrinsic MGS or by expression of the TME-specific
382 signature. Recently, the transcriptional GBM subtypes were redefined based on the
383 expression of glioma-intrinsic genes, thus excluding the genes expressed by cells of the
384 TME (Wang et al., 2017). Our master regulator analysis on the BTSCs points to the AP-
385 1 family member *FOSL1* as one of the top transcription factors contributing to the cell-
386 intrinsic MGS. Previous tumor bulk analysis identified a related AP-1 family member
387 *FOSL2*, together with *CEBPB*, *STAT3* and *TAZ*, as important regulators of the MES GBM
388 subtype (Bhat et al., 2011; Carro et al., 2010). While *FOSL1* was also listed as a putative
389 MES master regulator (Carro et al., 2010), its function and mechanism of action have not
390 been further characterized since then. Our experimental data show that *FOSL1* is a key

391 regulator of GBM subtype plasticity and MES transition, and define the molecular
392 mechanism through which *FOSLI* is regulated.

393 Although consistently defined, GBM subtypes do not represent static entities. The
394 plasticity between subtypes happens at several levels. Besides the referred MES-to-PN
395 change in cultured GSCs compared to the parental tumor (Bhat et al., 2013), a PN-to-
396 MES shift often occurs upon treatment and recurrence. Several independent studies
397 comparing matched pairs of primary and recurrent tumors demonstrated a tendency to
398 shift towards a MES phenotype, associated with a worse patient survival, likely as a result
399 of treatment-induced changes in the tumor and/or the microenvironment (Phillips et al.,
400 2006; Wang et al., 2016; Wang et al., 2017). Moreover, distinct subtypes/cellular states,
401 can coexist within the same tumor (Nefitel et al., 2019; Patel et al., 2014; Sottoriva et al.,
402 2013; Wang et al., 2019) and targeting these multiple cellular components could result in
403 more effective treatments (Wang et al., 2019).

404 PN-to-MES transition is often considered an EMT-like phenomenon, associated
405 with tumor progression (Fedele et al., 2019). The role of *FOSLI* in EMT has been studied
406 in other tumor types. In breast cancer cells *FOSLI* expression correlates with
407 mesenchymal features and drives cancer stem cells (Tam et al., 2013) and the regulation
408 of EMT seems to happen through the direct binding of FRA-1 to promoters of EMT genes
409 such as *Tgfb1*, *Zeb1* and *Zeb2* (Bakiri et al., 2015). In colorectal cancer cells, *FOSLI* was
410 also shown to promote cancer aggressiveness through EMT by direct transcription
411 regulation of EMT-related genes (Diesch et al., 2014; Liu et al., 2015).

412 It is well established that *NFI* inactivation is a major genetic event associated with
413 the MES subtype (Verhaak et al., 2010; Wang et al., 2017). However, this is probably a
414 late event in MES gliomagenesis, as all tumors possibly arise from a PN precursor and
415 just later in disease progression acquire *NFI* alterations that are directly associated with
416 a transition to a MES subtype (Ozawa et al., 2014). Moreover, *NFI* deficiency has been
417 recently linked to macrophage/microglia infiltration in the MES subtype (Wang et al.,
418 2017). The fact that the enriched macrophage/microglia microenvironment is also able to
419 modulate a MES phenotype suggests that there might be a two-way interaction between
420 tumor cells and TME. The mechanisms of NF1-regulated chemotaxis and whether this
421 relationship between the TME and MGS in GBM is causal remain elusive.

422 Here we provide evidence that manipulation of *NFI* expression levels in patient-
423 derived BTSCs has a direct consequence on the tumor-intrinsic MGS activation and that
424 such activation, can at least in part be mediated by the modulation of *FOSLI*. Among the

425 previously validated MRs, only *CEBPB* appears also to be finely modulated by *NFI*
426 inactivation. This suggests that among the TFs previously characterized (such as *FOSL2*,
427 *STAT3*, *BHLHB2* and *RUNX1*), *FOSL1* and *CEBPB* might play a specific role in the *NFI*-
428 mediated MES transition that occurs in glioma cells with limited or possibly absent effect
429 by the TME. However, whether *FOSL1* contributes also to the putative cross-talk between
430 the TME and the cell-intrinsic MGS, will still have to be established.

431 Furthermore we show that *FOSL1* is a crucial player in glioma pathogenesis,
432 particularly in a MAPK-driven MES GBM context. Our findings broaden its previously
433 described role in KRAS-driven epithelial tumors, such as lung and pancreatic ductal
434 adenocarcinoma (Vallejo et al., 2017). *NFI* inactivation results in Ras activation, which
435 stimulates downstream pathways as MAPK and PI3K/Akt /mTOR. RAS/MEK/ERK
436 activation in turn regulates *FOSL1* mRNA expression and FRA-1 protein stability
437 (Casalino et al., 2003; Verde et al., 2007). FRA-1 can then directly bind and activate some
438 of the MES genes, while possibly binding its own promoter to activate its own expression
439 (Diesch et al., 2014; Lau et al., 2016). This generates a feedback loop that induces MGS,
440 increases proliferation and stemness, sustaining tumor growth. FRA-1 requires, for its
441 transcriptional activity, heterodimerization with the AP-1 transcription factors JUN,
442 JUNB or JUND (Eferl and Wagner, 2003). Which of the JUN family members participate
443 in the MES gene regulation and whether FRA-1 activates MES gene expression and
444 simultaneously represses PN genes, requires further investigation.

445 In conclusion, *FOSL1* is a master regulator of the MES subtype of GBM,
446 significantly contributing to its stem cell features, which could open new therapeutic
447 options. Although *FOSL1* pharmacological inhibition is difficult to achieve due to the
448 lack of specific inhibitors, a gene therapy approach targeting *FOSL1* expression through
449 CRISPR, for instance, could constitute an attractive alternative to treat MES GBM
450 patients.

451

452 **Acknowledgements**

453 We would like to thank Álvaro Ucero for his input on the project and Flora A.
454 Díaz for her technical support. We are grateful to Francisco X. Real and Scott Lowe for
455 critical input on the manuscript. We thank Pamela Franco for experimental support and
456 discussion. This work was supported by a grant from the Marie Curie International re-
457 integration Grants (MC-IRG), project nr. 268303 (to M.S.C.) and by grants from the

458 ISCH3, project PI13/01028, cofounded by the European Regional Development Fund
459 (ERDF), and from the Seve Ballesteros Foundation (to M.S.).

460

461 **Author Contributions**

462 C.M designed and performed experiments, analyzed data and wrote the
463 manuscript. T.U., P.K., A.I. and E.K. performed experiments. G.G. analyzed data and
464 interpreted experiments. O.S. provided tumor samples. S.N. provided cell lines. L.B. and
465 E.F.W. provided reagents, contributed to experimental design and interpreted
466 experiments. M.S.C and M.S. conceived the project, designed and interpreted
467 experiments and wrote the manuscript.

468

469 **Declaration of interests**

470 The authors declare no competing interests.

471

472 **Material and Methods**

473 **Generation of the BTSCs dataset and Master regulator analysis (MRA)**

474 The brain tumor stem cell lines (BTSCs) dataset was assembled with new and previously
475 generated transcriptomic data: 24 Illumina HumanHT-12v4 expression BeadChip
476 microarrays newly generated at Freiburg University (GSE137310, this study); 44 RNA-
477 seq samples (Illumina HiSeq 2500) from GSE119834 (Mack et al., 2019), 30 Affymetrix
478 Human Genome U219 microarrays from GSE67089 (Mao et al., 2013) and 17 Affymetrix
479 HG-U133 Plus 2.0 microarrays from GSE8049 (Günther et al., 2008). For the previously
480 published data, at exception of the GSE119834, for which pre-processed data were used,
481 raw data were downloaded from the GEO repository
482 (<https://www.ncbi.nlm.nih.gov/geo/>) and subsequently the ‘affy’ package (R
483 programming language) was used for robust multi-array average normalization followed
484 by quantile normalization. For genes with several probe sets, the median of all probes had
485 been chosen and only common genes among all the datasets (n = 14821) were used for
486 further analysis. To avoid issues with the use of different transcriptomic platforms each
487 dataset was then scaled (mean = 0, sd = 1) before assembling the combined final dataset.
488 Transcriptional subtypes were obtained using the ‘ssgsea.GBM.classification’ R package
489 (Wang et al., 2017), through the SubtypeME tool of the GlioVis web portal

490 (<http://gliovis.bioinfo.cnio.es>) (Bowman et al., 2017). Differential gene expression (MES
491 vs Non-MES BTSCs) was performed using the ‘limma’ R package.

492 The master regulator analysis was performed using the ‘RTN’ R package (Castro
493 et al., 2016). Normalized BTSC expression data were used as input to build a
494 transcriptional network (TN) for 785 TFs present in the dataset. TF annotations were
495 obtained from Gene Ontology (GO:0003700). P values for network edges were computed
496 from a pooled null distribution using 1000 permutations. Edges with an adjusted-P value
497 < 0.05 were kept for data processing inequality (DPI) filtering. In the TN, each target can
498 be connected to multiple TFs and regulation can occur as a result of both direct and
499 indirect interactions. DPI-filtering removes the weakest interaction in any triangle of two
500 TFs and a target gene, therefore preserving the dominant TF-target pairs and resulting in
501 a filtered TN that highlights the most significant interactions (Fletcher et al., 2013). Post-
502 DPI filtering, the MRA computes the overlap between the transcriptional regulatory
503 unities (regulons) and the input signature genes using the hypergeometric distribution
504 (with multiple hypothesis testing corrections). To identify master regulators, the
505 differential gene expression between MES and Non-MES was used as a phenotype.

506

507 **TCGA pan-glioma data analysis**

508 RSEM normalized RNA-seq data for the TCGA GBMLGG dataset were
509 downloaded from the Broad Institute Firebrowse (<http://gdac.broadinstitute.org>). *NFI*
510 copy number alterations and point mutations were obtained at the cBioPortal
511 (<https://www.cbioportal.org>). Transcriptional subtypes were inferred using the
512 ‘*ssgsea.GBM.classification*’ R package as indicated above. Glioma molecular subtypes
513 information was downloaded from the GlioVis web portal (<http://gliovis.bioinfo.cnio.es>)
514 (Bowman et al., 2017). Survival analysis was performed using the ‘survival’ R package.

515

516 **Gene Expression Array and gene set enrichment analysis (GSEA)**

517 For gene expression profiling of the BTSC lines of the Freiburg dataset, total RNA
518 was prepared using the RNeasy kit (Qiagen #74104) or the AllPrep DNA/RNA/Protein
519 mini kit (Qiagen #80004) and quantified using 2100 Bioanalyzer (Agilent). One-and-a-
520 half μg of total RNA for each sample was sent to the genomic facility of the German
521 Cancer Research Center (DKFZ) in Heidelberg (Germany) where hybridization and data
522 normalization were performed. Hybridization was carried out on Illumina HumanHT-

523 12v4 expression BeadChip. Gene set enrichment analysis was performed using the GSEA
524 software (<http://www.broadinstitute.org/gsea/index.jsp>).

525

526 **ChIP-seq analysis**

527 We downloaded FOSL1 ChIP-seq profiling from ENCODE tracks ENCFF000OZR and
528 ENCFF000OZQ. OLIG2 binding sites and ChIP-seq profiles were downloaded from
529 GEO: GSM1306365_MGG8TPC.OLIG2r1c and GSM1306367_MGG8TPC.OLIG2r2.
530 H3K27Ac data were downloaded from GSE119755 (Mack et al., 2019) for
531 GSM3382291_GSC17, GSM3382343_GSC40, GSM3382319_GSC3,
532 GSM3382321_GSC30, GSM3382341_GSC4, GSM3382277_GSC10. Scatter plots were
533 generated with Seqmonk v1.45 using FOSL1 binding sites in MES-BTSCs using a
534 Kolmogorov-Smirnov test with a sample size of 297 when constructing the control
535 distributions and filtering by maximum P value of 0.05 (multiple testing correction
536 applied). Minimum absolute z-score was 0.5. A custom regression was calculated.
537 Quantitation was Read Count Quantitation using all reads correcting for total count only
538 in probes to largest store log transformed duplicates ignored. Heatmaps were generated
539 using ChaSE, using either FOSL1 or OLIG2 binding sites with $\pm 10,000$ bp.

540

541 **Mouse strains and husbandry**

542 *GFAP-tv-a*; *hGFAP-Cre*; *Rosa26-LSL-Cas9* mice were previously described
543 (Oldrini et al., 2018). *Kras^{LSLG12V}*; *Trp53^{lox}*; *Rosa26^{LSLrtTA-IRES-EGFP}*; *Colla1^{TetO-Fos11}*
544 mouse strain corresponds to the MGI Allele References 3582830, 1931011, 3583817 and
545 5585716, respectively. Immunodeficient *nu/nu* mice (MGI: 1856108) were obtained at
546 the Spanish National Cancer Research Centre Animal Facility.

547 Mice were housed in the specific pathogen-free animal house of the Spanish
548 National Cancer Research Centre under conditions in accordance with the
549 recommendations of the Federation of European Laboratory Animal Science
550 Associations (FELASA). All animal experiments were approved by the Ethical
551 Committee (CElyBA) and performed in accordance with the guidelines stated in the
552 International Guiding Principles for Biomedical Research Involving Animals, developed
553 by the Council for International Organizations of Medical Sciences (CIOMS).

554

555 **Cell lines and cell culture**

556 Mouse neural stem cells (NSCs) were derived from the whole brain of newborn
557 mice of *Gtv-a*; *hGFAP-Cre*; *LSL-Cas9*; *Trp53^{lox}* (referred as p53-null NSCs) and
558 *Kras^{LSLG12V}*; *Trp53^{lox}*; *Rosa26^{LSLrtTA-IRES-EGFP}*; *Colla1^{TetO-FosII}* (referred as *FosII^{TetON}*
559 NSCs). Tumorsphere lines were derived from tumors of C57BL/6J injected with
560 *FosII^{TetON}* NSCs, when mice were sacrificed after showing symptoms of brain tumor
561 disease. For the derivation of mouse NSCs and tumorspheres, tissue was enzymatically
562 digested with 5 mL of papain digestion solution (0.94 mg/mL papain (Worthington
563 #LS003119), 0.48 mM EDTA, 0.18 mg/mL N-acetyl-L-cysteine (Sigma-Aldrich
564 #A9165) in Earl's Balanced Salt Solution (Gibco #14155-08)) and incubated at 37°C for
565 8 min. After digestion, the enzyme was inactivated by the addition of 2 mL of 0.71 mg/mL
566 ovomucoid (Worthington #LS003087) and 0.06 mg/mL DNaseI (Roche #10104159001)
567 diluted in Mouse NeuroCult basal medium (Stem Cell Technologies #05700) without
568 growth factors. Cell suspension was centrifuged at a low speed and then passed through
569 a 40 µm mesh filter to remove undigested tissue, washed first with PBS and then with
570 ACK lysing buffer (Gibco #A1049201) to remove red blood cells. NSCs and
571 tumorspheres were grown in Mouse NeuroCult basal medium, supplemented with
572 Proliferation supplement (Stem Cell Technologies #05701), 20 ng/mL recombinant
573 human EGF (Gibco #PHG0313), 10 ng/mL basic-FGF (Millipore #GF003-AF), 2 µg/mL
574 Heparin (Stem Cell Technologies #07980) and L-glutamine (2mM, Hyclone
575 #SH3003401). Spheres were dissociated with Accumax (ThermoFisher Scientific #00-
576 4666-56) and re-plated every 4-5 days.

577 Patient-derived glioblastoma stem cells (BTSCs) were prepared from tumor
578 specimens under IRB-approved guidelines as described before (Fedele et al., 2017).
579 BTSCs were grown as neurospheres in Neurobasal medium (Gibco #10888022)
580 containing B27 supplement (Gibco #12587010), N2 supplement (Gibco #17502048), b-
581 FGF (20 ng/mL), EGF (20 ng/mL), LIF (10 ng/mL, CellGS #GFH200-20), 2 µg/mL
582 Heparin and L-glutamine (2mM). JX6 were kindly provided by Y. Gillespie (UAB,
583 Birmingham).

584

585 **Vectors, virus production and infection**

586 Flag-tagged NF1-GRD (aminoacids 1131-1534) was amplified by PCR from
587 human cortical tissue (epilepsy patient) and first cloned in the pDRIVE vector. Primers
588 are listed in Table S5. The NF1-GRD sequence was then excised by restriction digestion
589 using PmeI and SpeI enzymes and subcloned in the modified pCHMWS lentiviral vector

590 (kind gift from V. Baekelandt, University of Leuven, Belgium) sites by removing the
591 *fluc* region. The correct sequence was verified by sequencing. For *NFI* silencing, *NFI*
592 short hairpin from pLKO (Sigma, TRCN0000238778) vector was subcloned in pGIPZ
593 lentiviral vector (Open Biosystems). The corresponding short hairpin sequence was
594 synthesized (GATC) and amplified by PCR using XhoI and EcoRI sites containing
595 primers. The PCR product was digested using XhoI and EcoRI and subcloned into the
596 pGIPZ vector previously digested with XhoI and PmeI following by digestion with
597 EcoRI. The two vector fragments were ligated with *NFI* short hairpin fragment. The
598 correct insertion and sequence was validated by sequencing. In addition, experiments
599 were performed using sh*NFI*-pGIPZ clone V2LHS_76027 (clone 4) and V2LHS_260806
600 (clone 5).

601 RCAS viruses (RCAS-sh*Nfi*, RCAS-sg*Nfi* and RCAS-*Kras*^{G12V}) used for
602 infection of p53-null NSCs were obtained from previously transfected DF1 chicken
603 fibroblasts (ATCC #CRL-12203) using FuGENE 6 Transfection reagent (Promega
604 #E2691), according to manufacturer's protocol. DF1 cells were grown at 39°C in DMEM
605 containing GlutaMAX™ (Gibco #31966-021) and 10% FBS (Sigma-Aldrich #F7524).

606 The pKLV-U6gRNA-PGKpuro2ABFP was a gift from Dr. Kosuke Yusa
607 (Wellcome Sanger Institute) (Addgene plasmid #50946). For cloning of single gRNAs,
608 oligonucleotides containing the BbsI site and the specific gRNA sequences were
609 annealed, phosphorylated and ligated into the pKLV-U6gRNA(BbsI)-PGKpuro2ABFP
610 previously digested with BbsI. Single gRNAs to target *Fosll* were designed with Guide
611 Scan (<http://www.guidescan.com/>) and the sequences cloned were sg*Fosll*_1:
612 TACCGAGACTACGGGAACC; sg*Fosll*_2: CCTAGGGCTCGTATGACTCC;
613 sg*Fosll*_3: ACCGTACGGGCTGCCAGCCC. These vectors and a non-targeting sgRNA
614 control were used to transduce p53-null *Kras*^{G12V} NSCs.

615 The pLVX-Cre and respective control vector were kindly provided by Dr. Maria
616 Blasco (CNIO) and used to transduce *Fosll*^{TetON} NSCs; pLKO.1-TET-sh*FOSL1* and
617 respective control vector were a gift from Dr. Silve Vicent (CIMA, Navarra University).

618 Gp2-293 packaging cell line (Clontech #631458) was grown in DMEM (Sigma-
619 Aldrich #D5796) with 10% FBS. Lentiviruses generated in this cell line were produced
620 using calcium-phosphate precipitate transfection and co-transfected with second-
621 generation packaging vectors (pMD2G and psPAX2). High-titer virus was collected at
622 36 and 60 h following transfection.

623 All cells were infected with lenti- or retroviruses by four cycles of spin infection
624 ($200 \times g$ for 2 h), in presence of 8 $\mu\text{g}/\text{mL}$ polybrene (Sigma-Aldrich #H9268). Transduced
625 cells were selected after 48 h from the last infection with 1 $\mu\text{g}/\text{mL}$ Puromycin (Sigma-
626 Aldrich #P8833).

627

628 **Generation of murine gliomas**

629 p53-null *Kras*^{G12V} NSCs (5×10^5 cells) were injected intracranially into 4 to 5
630 weeks-old immunodeficient *nu/nu* mice.

631 *FosII*^{TetON} NSCs (5×10^5 cells) were intracranially injected into 4 to 5 weeks-old
632 wildtype C57Bl/6J mice that were fed *ad libitum* with 2 g/kg doxycycline-containing
633 pellets. Due to the limited penetration of the blood brain barrier and to insure enough Dox
634 was reaching the brain, 2 mg/mL Dox (PanReac AppliChem #A29510025) was also
635 added to drinking water with 1% sucrose (Sigma-Aldrich #S0389) (Annibali et al., 2014;
636 Mansuy and Bujard, 2000). Control mice were kept with regular food and 1% sucrose
637 drinking water.

638 Mice were anaesthetized with 4% isoflurane and then injected with a stereotactic
639 apparatus (Stoelting) as previously described (Hambardzumyan et al., 2009). After
640 intracranial injection, all mice were routinely checked and sacrificed when developed
641 symptoms of disease (lethargy, poor grooming, weight loss and macrocephaly).

642

643 **Immunohistochemistry**

644 Tissue samples were fixed in 10% formalin, paraffin-embedded and cut in 3 μm
645 sections, which were mounted in Superfrost Plus microscope slides (Thermo Scientific
646 #J1810AMNZ) and dried. Tissues were deparaffinized in xylene and re-hydrated through
647 graded concentrations of ethanol in water, ending in a final rinse in water.

648 For histopathological analysis, sections were stained with hematoxylin and eosin
649 (H&E).

650 For immunohistochemistry, deparaffinized sections underwent heat-induced
651 antigen retrieval, endogenous peroxidase activity was blocked with 3% hydrogen
652 peroxide (Sigma-Aldrich #H1009) for 15 min and slides were then incubated in blocking
653 solution (2.5% BSA (Sigma-Aldrich #A7906) and 10% Goat serum (Sigma-Aldrich
654 #G9023), diluted in PBS) for at least 1 h. Incubations with anti-FRA-1 (Santa Cruz #sc-
655 183, 1:100) and anti-CD44 (BD Biosciences #550538, 1:100) were carried out overnight
656 at 4°C. Slides were then incubated with secondary anti-rabbit (Vector #BA-1000) or anti-

657 rat (Vector #BA-9400) for 1 h at RT and with AB (avidin and biotinylated peroxidase)
658 solution (Vectastain Elite ABC HRP Kit, Vector, PK-6100) for 30 min. Slides were
659 developed by incubation with peroxidase substrate DAB (Vector SK-4100) until desired
660 stain intensity. Finally, slides were counterstained with hematoxylin, cleared and
661 mounted with a permanent mounting medium.

662 Immunohistochemistry for S100A4 (Abcam #ab27957, 1:300) and Ki67 (Master
663 Diagnostica #0003110QD, undiluted) was performed using an automated
664 immunostaining platform (Ventana discovery XT, Roche).

665

666 **Immunoblotting**

667 Cell pellets or frozen tumor tissues were lysed with JS lysis buffer (50 mM
668 HEPES, 150 mM NaCl, 1% Glycerol, 1% Triton X-100, 1.5 mM MgCl₂, 5 mM EGTA)
669 and protein concentrations were determined by DC protein assay kit II (Bio-Rad
670 #5000112). Proteins were separated on house-made SDS-PAGE gels and transferred to
671 nitrocellulose membranes (Amersham #10600003). Membranes were incubated in
672 blocking buffer (5% milk in TBST) and then with primary antibody overnight at 4°C. The
673 following primary antibodies and respective dilutions were used: FLAG (Cell Signaling
674 Technology #2368S, 1:2000), FRA-1 (Santa Cruz #sc-183, 1:1000; #sc-605, 1:1000),
675 GFAP (Sigma-Aldrich #G3893, 1:5000), NF1 (Santa Cruz #sc-67, 1:500; Bethyl #A300-
676 140A, 1:1000), OLIG2 (Millipore #AB9610, 1:2000), VIMENTIN (Cell Signaling
677 Technology #5741, 1:3000), p-ERK1/2 (T202/Y204) (Cell Signaling Technology, #9101,
678 1:2000/3000; Assay Designs #ADI-905-651, 1:250), ERK1/2 (Cell Signaling
679 Technology, #9102, 1:1000; Abcam #ab17942, 1:1000), p-MEK (S217/221) (Cell
680 Signaling Technology, #9154, 1:500/1000), MEK (Cell Signaling Technology, #9122
681 1:1000), CHI3L1 (Qidel #4815, 1:1000), p85 (Millipore #06-195, 1:10000), VINCULIN
682 (Sigma-Aldrich #V9131, 1:10000) and α -TUBULIN (Abcam #ab7291, 1:10000). Anti-
683 mouse or rabbit-HRP-conjugated antibodies (Jackson ImmunoResearch, #115-035-003
684 and #111-035-003) were used to detect desired protein by chemiluminescence with ECL
685 Detection Reagent (Amersham, #RPN2106).

686

687 **Reverse transcription quantitative PCR**

688 RNA from NSCs and frozen tissue was isolated with TRIzol reagent (Invitrogen
689 #15596-026) according to the manufacturer's instructions. For reverse transcription PCR
690 (RT-PCR), 500 ng of total RNA was reverse transcribed using the High Capacity cDNA

691 Reverse Transcription Kit (Applied Biosystems #4368814). Quantitative PCR was
692 performed using the SYBR Select Master Mix (Applied Biosystems #4472908) according
693 to the manufacturer's instructions. qPCRs were run and the melting curves of the
694 amplified products were used to determine the specificity of the amplification. The
695 threshold cycle number for the genes analyzed was normalized to GAPDH. Mouse and
696 human primer sequences are listed in Table S5.

697 RNA from BTSC cells was prepared using the RNeasy kit or the AllPrep
698 DNA/RNA Protein Mini Kit and used for first strand cDNA synthesis using random
699 primers and SuperscriptIII reverse transcriptase (Life Technologies #18080-085). Primer
700 sequences used in qRT-PCR with SYBR Green are listed in Table S5. Quantitative real-
701 time PCR (qRT-PCR) STAT3 and CEBPB were performed using pre-validated TaqMan
702 assays (Applied Biosystems): STAT3: Hs01047580, CEBPB: Hs00270923 and 18s
703 rRNA: Hs99999901.

704

705 **MTT assay**

706 Cells were seeded in 96-well culture plates (1000 cells per well, 10 wells per cell
707 line) and grown for 7 days. At each timepoint (days 1, 3, 5 and 7), cell viability was
708 determined by MTT assay. Briefly, 10 μ L of 5 mg/mL MTT (Sigma-Aldrich #M5655)
709 was added to each well and cells were incubated for 4 h before lysing with a formazan
710 solubilization solution (10% SDS in 0.01 M HCl). Colorimetric intensity was quantified
711 using a plate reader at 590 nm. Values were obtained after subtraction of matched blanks
712 (medium only).

713

714 **Cell cycle analysis: Propidium iodide (PI) staining**

715 Cells were harvested and washed twice with PBS prior to fixation with 70% cold
716 ethanol, added drop-wise to the cell pellet while vortexing. Fixed cells were then washed,
717 first with 1% BSA in PBS, then with PBS only and stained overnight with 50 μ g/mL PI
718 (Sigma-Aldrich #P4170) and 100 μ g/mL RNase A (Roche #10109142001) in PBS.
719 Samples were acquired in a FACSCanto II cytometer (BD Biosciences) and data were
720 analyzed using FlowJo software.

721

722 **BrdU incorporation**

723 Cells were pulse-labelled with 10 μ M BrdU (Sigma-Aldrich #B9285) for 2 h,
724 harvested and washed twice with PBS prior to fixation with 70% ethanol cold ethanol,

725 added drop-wise to the cell pellet while vortexing. DNA denaturation was performed by
726 incubating samples for 10 min on ice with 0.1 M HCl with 0.5% Tween-20 and samples
727 were then resuspended in water and boiled at 100°C for 10 min. Anti-BrdU-FITC
728 antibody (BD Biosciences #556028) was incubated according to manufacturer's protocol.
729 After washing with PBSTB (PBS with 0.5% Tween-20 and 1% BSA), samples were
730 resuspended in 25 µg/mL PI and 100 µg/mL RNase A diluted in PBS. Samples were
731 acquired in a FACSCanto II cytometer (BD Biosciences) and data were analyzed using
732 FlowJo software.

733

734 **Immunofluorescence**

735 Cells were plated in laminin-coated coverslips and fixed with 4% PFA for 15 min.
736 Cells were then permeabilized with 0.1% Triton X-100 in 0.2% BSA and coverslips were
737 washed and blocked with 10% donkey serum in 0.2% BSA for 1 h. The following primary
738 antibodies were incubated overnight at 4°C: CD44 (BD Biosciences #550538, 1:100),
739 GFAP (Millipore #MAB360, 1:400) and OLIG2 (Millipore #AB9610, 1:100). Secondary
740 antibodies at 1:400 dilution (from Invitrogen, Alexa-Fluor anti-rabbit-488, anti-mouse-
741 488 and anti-rat 594) were incubated for 1 h at RT and after washing coverslips were
742 incubated for 4 min with DAPI (1:4000, Sigma-Aldrich #D8417) and mounted with
743 ProLong Gold Antifade reagent (Invitrogen #P10144).

744 Fluorescence signal was quantified as the ratio of green/red pixel area relative to
745 DAPI pixel area per field of view, in a total of 36 fields per condition analyzed.

746

747 **Neurosphere formation assay and limiting dilution analysis**

748 Neurospheres were dissociated and passed through a 40 µm mesh filter to
749 eliminate non-single cells. Decreasing cell densities were plated in ultra-low attachment
750 96-well plates (Corning #CLS3474) and fresh medium was added every 3-4 days. The
751 number of positive wells for presence of spheres was counted 2 weeks after plating.
752 Limiting dilution analysis was performed using ELDA R package
753 (<http://bioinf.wehi.edu.au/software/elda/>).

754

755 **RNA-sequencing and analysis on mouse NSCs**

756 One microgram of total RNA from the samples was used. cDNA libraries were
757 prepared using the "QuantSeq 3' mRNA-Seq Library Prep Kit (FWD) for Illumina"
758 (Lexogen #015) by following manufacturer instructions. Library generation is initiated

759 by reverse transcription with oligo(dT) priming, and a second strand synthesis is
760 performed from random primers by a DNA polymerase. Primers from both steps contain
761 Illumina-compatible sequences. Adapter-ligated libraries were completed by PCR,
762 applied to an Illumina flow cell for cluster generation and sequenced on an Illumina
763 HiSeq 2500 by following manufacturer's protocols. Sequencing read alignment and
764 quantification and differential gene expression analysis was performed in the Bluebee
765 Genomics Platform, a cloud-based service provider (www.bluebee.com). Briefly, reads
766 were first trimmed with bbdduk from BBTools (BBMap – Bushnell B,
767 <https://sourceforge.net/projects/bbmap/>) to remove adapter sequences and polyA tails.
768 Trimmed reads were aligned to the GRCm38/mm10 genome assembly with STAR v 2.5
769 (Dobin et al., 2013). Read counting was performed with HTSeq (Anders et al., 2015).
770 Differential gene expression analysis was performed with DESeq2 (Love et al., 2014).
771 The list of stem/differentiation markers was compiled by combining a previously
772 described gene list (Sandberg *et al.* 2013) with other markers (Bazzoli et al., 2012).
773 GSEAPreranked (Subramanian et al., 2005) was used to perform gene set enrichment
774 analysis of the described indicated signatures on a pre-ranked gene list, setting 1000 gene
775 set permutations.

776

777 **Osteogenesis Differentiation Assay**

778 The osteogenesis differentiation assay was performed using the StemPro
779 Osteogenesis Differentiation Kit (Life Technologies #A1007201) according to the
780 manufacturer's instructions. Briefly, 5×10^3 cells/cm² were seeded on laminin-coated
781 glass coverslips in a 24-well cell culture plate. Cells were incubated in MSC Growth
782 Medium at 37°C, 5% CO₂ for 21 days, replacing the medium every 4 days. Cells were
783 then fixed with 4% formaldehyde, stained with Alizarin Red S solution (pH 4.2) and
784 mounted on microscope slides. Pictures were acquired using an Axiovert Microscope
785 (Zeiss).

786

787 **Active Ras pull down assay**

788 Active Ras pull down assay was performed using Active Ras pull down assay kit
789 (ThermoFisher Scientific #16117) according to the manufacturer's instructions. Briefly,
790 cells were grown in 10 cm plates at 80-90% confluency in presence or absence of growth
791 factors (EGF, FGF and LIF), and lysed with the provided buffer. Lysates were incubated

792 with either GDP or GTP for 30 min followed by precipitation with GST-Raf1-RBD.
793 Western blot was performed with the provided anti-RAS antibody (1:250).

794

795 **Chromatin preparation and FRA-1 ChIP**

796 BTSC cells were collected at 2×10^6 cells confluency, washed in PBS and fixed by
797 addition of 1% formaldehyde for 20 min at room temperature. The cells were resuspended
798 in 2 mL Lysis Buffer (50 mM Tris pH 7.5; 1 mM EDTA pH 8.0; 1% Triton; 0.1% Na-
799 deoxycholate; 150 mM NaCl; protease inhibitors) on ice for 20 min. The suspension was
800 sonicated in a cooled Bioruptor Pico (Diagenode), and cleared by centrifugation for 10
801 min at 13000 rpm. The chromatin (DNA) concentration was quantified using NanoDrop
802 (Thermo Scientific) and the sonication efficiency monitored on an agarose gel. Protein
803 A/G plus-agarose beads (Santa Cruz #sc-2003) were blocked with sonicated salmon
804 sperm (ThermoFisher #AM9680, 200 mg/mL beads) and BSA (NEB #B9000S, 250
805 mg/mL beads) in dilution buffer (0.5% NP40; 200 mM NaCl; 50 mM Tris pH 8.0;
806 protease inhibitors) for 2 h at room temperature. The chromatin was pre-cleared with 80
807 μ L of blocked beads for 1 h at 4°C. Pre-cleared chromatin was incubated with 5 μ g of
808 FRA-1 antibody (Santa Cruz #sc-605) overnight at 4°C, then with 40 μ L of blocked beads
809 for further 2 h at 4°C. Control mock immunoprecipitation was performed with blocked
810 beads. The beads were washed 1 \times with Wash1 (20 mM Tris pH 7.5; 2 mM EDTA pH
811 8.0; 1% Triton; 0.1% SDS; 150 mM NaCl), 1 \times with Wash2 (20 mM Tris pH 7.5; 2 mM
812 EDTA pH 8.0; 1% Triton; 0.1% SDS; 500 mM NaCl), 1 \times with LiCl Wash (20 mM Tris
813 pH 7.5; 1 mM EDTA pH 8.0; 1% NP40; 1% deoxycholate; 250 mM LiCl) and 2 \times in TE
814 (10 mM Tris pH 7.5; 1 mM EDTA). The immuno-complexes were eluted by two 15 min
815 incubations at 30°C with 100 μ L Elution buffer (1% SDS, 100 mM NaHCO₃), and de-
816 crosslinked overnight at 65°C in the presence of 10 U RNase A (Ambion #AM9780). The
817 immune-precipitated DNA was then purified with the QIAquick PCR purification kit
818 (Qiagen #28104) according to manufacturer's protocol and analyzed by quantitative real-
819 time PCR.

820

821 **Statistical analysis**

822 All statistical analyses were performed using R programming language. Statistical
823 differences between groups in the *in vitro* assays were assessed by unpaired two-tailed
824 Student's t tests, unless otherwise specified.

825 Kaplan–Meier survival curves were produced with GraphPad Prism and P values
826 were generated using the Log-Rank statistics.

827 Results are presented as mean \pm standard deviation (SD), and statistical
828 significance was defined as $P \leq 0.05$ for a 95% confidence interval.

829

830 **Data and code availability**

831 The accession numbers for data reported in this paper are GEO: GSE137310
832 (Freiburg BTSCs) and GSE138010 (mouse NSCs). All the code used for data analysis
833 and plots generation will be available at: <https://github.com/squattrim/Marques2019>.

834

835

836 **References**

837 Anders, S., Pyl, P.T., and Huber, W. (2015). HTSeq--a Python framework to work with
838 high-throughput sequencing data. *Bioinformatics* 31, 166–169.

839 Andreolas, C., Kalogeropoulou, M., Voulgari, A., and Pintzas, A. (2008). Fra-1
840 regulates vimentin during Ha-RAS-induced epithelial mesenchymal transition in
841 human colon carcinoma cells. *Int. J. Cancer* 122, 1745–1756.

842 Annibaldi, D., Whitfield, J.R., Favuzzi, E., Jauset, T., Serrano, E., Cuartas, I., Redondo-
843 Campos, S., Folch, G., González-Juncà, A., Sodik, N.M., et al. (2014). Myc inhibition is
844 effective against glioma and reveals a role for Myc in proficient mitosis. *Nat. Commun.*
845 5, 1–11.

846 Bakiri, L., MacHo-Maschler, S., Custic, I., Niemiec, J., Guió-Carrión, A., Hasenfuss,
847 S.C., Eger, A., Müller, M., Beug, H., and Wagner, E.F. (2015). Fra-1/AP-1 induces
848 EMT in mammary epithelial cells by modulating Zeb1/2 and TGF β expression. *Cell*
849 *Death Differ.* 22, 336–350.

850 Bao, S., Wu, Q., McLendon, R.E., Hao, Y., Shi, Q., Hjelmeland, A.B., Dewhirst, M.W.,
851 Bigner, D.D., and Rich, J.N. (2006). Glioma stem cells promote radioresistance by
852 preferential activation of the DNA damage response. *Nature* 444, 756–760.

853 Basso, K., Margolin, A.A., Stolovitzky, G., Klein, U., Dalla-Favera, R., and Califano,
854 A. (2005). Reverse engineering of regulatory networks in human B cells. *Nat. Genet.*
855 37, 382–390.

856 Bazzoli, E., Pulvirenti, T., Oberstadt, M.C., Perna, F., Wee, B., Schultz, N., Huse, J.T.,
857 Fomchenko, E.I., Voza, F., Tabar, V., et al. (2012). MEF Promotes Stemness in the
858 Pathogenesis of Gliomas. *Cell Stem Cell* 11, 836–844.

859 Belteki, G., Haigh, J., Kabacs, N., Haigh, K., Sison, K., Costantini, F., Whitsett, J.,
860 Quaggin, S.E., and Nagy, A. (2005). Conditional and inducible transgene expression in
861 mice through the combinatorial use of Cre-mediated recombination and tetracycline
862 induction. *Nucleic Acids Res.* 33, 1–10.

863 Bhat, K.P.L., Salazar, K.L., Balasubramanian, V., Wani, K., Heathcock, L.,
864 Hollingsworth, F., James, J.D., Gumin, J., Diefes, K.L., Kim, S.H., et al. (2011). The
865 transcriptional coactivator TAZ regulates mesenchymal differentiation in malignant

- 866 glioma. *Genes Dev.* *25*, 2594–2609.
- 867 Bhat, K.P.L., Balasubramaniyan, V., Vaillant, B., Ezhilarasan, R., Hummelink, K.,
868 Hollingsworth, F., Wani, K., Heathcock, L., James, J.D., Goodman, L.D., et al. (2013).
869 Mesenchymal Differentiation Mediated by NF- κ B Promotes Radiation Resistance in
870 Glioblastoma. *Cancer Cell* *24*, 331–346.
- 871 Bowman, R.L., Wang, Q., Carro, A., Verhaak, R.G.W., and Squatrito, M. (2017).
872 GlioVis data portal for visualization and analysis of brain tumor expression datasets.
873 *Neuro. Oncol.* *19*, 139–141.
- 874 Brennan, C.W., Verhaak, R.G.W., McKenna, A., Campos, B., Noushmehr, H., Salama,
875 S.R., Zheng, S., Chakravarty, D., Sanborn, J.Z., Berman, S.H., et al. (2013). The
876 somatic genomic landscape of glioblastoma. *Cell* *155*, 462–477.
- 877 Carro, M.S., Lim, W.K., Alvarez, M.J., Bollo, R.J., Zhao, X., Snyder, E.Y., Sulman,
878 E.P., Anne, S.L., Doetsch, F., Colman, H., et al. (2010). The transcriptional network for
879 mesenchymal transformation of brain tumours. *Nature* *463*, 318–325.
- 880 Casalino, L., De Cesare, D., and Verde, P. (2003). Accumulation of Fra-1 in ras-
881 Transformed Cells Depends on Both Transcriptional Autoregulation and MEK-
882 Dependent Posttranslational Stabilization. *Mol. Cell. Biol.* *23*, 4401–4415.
- 883 Castro, M.A.A., de Santiago, I., Campbell, T.M., Vaughn, C., Hickey, T.E., Ross, E.,
884 Tilley, W.D., Markowitz, F., Ponder, B.A.J., and Meyer, K.B. (2016). Regulators of
885 genetic risk of breast cancer identified by integrative network analysis. *Nat. Genet.* *48*,
886 12–21.
- 887 Ceccarelli, M., Barthel, F.P., Malta, T.M., Sabedot, T.S., Salama, S.R., Murray, B.A.,
888 Morozova, O., Newton, Y., Radenbaugh, A., Pagnotta, S.M., et al. (2016). Molecular
889 Profiling Reveals Biologically Discrete Subsets and Pathways of Progression in Diffuse
890 Glioma. *Cell* *164*, 550–563.
- 891 Chen, J., Li, Y., Yu, T.S., McKay, R.M., Burns, D.K., Kernie, S.G., and Parada, L.F.
892 (2012). A restricted cell population propagates glioblastoma growth after chemotherapy.
893 *Nature* *488*, 522–526.
- 894 Chiappetta, G., Ferraro, A., Botti, G., Monaco, M., Pasquinelli, R., Vuttariello, E.,

- 895 Arnaldi, L., Di Bonito, M., D’Aiuto, G., Pierantoni, G.M., et al. (2007). FRA-1 protein
896 overexpression is a feature of hyperplastic and neoplastic breast disorders. *BMC Cancer*
897 *7*, 17.
- 898 Cooper, L.A.D., Gutman, D.A., Chisolm, C., Appin, C., Kong, J., Rong, Y., Kurc, T.,
899 Van Meir, E.G., Saltz, J.H., Moreno, C.S., et al. (2012). The Tumor Microenvironment
900 Strongly Impacts Master Transcriptional Regulators and Gene Expression Class of
901 Glioblastoma. *Am. J. Pathol.* *180*, 2108–2119.
- 902 Debinski, W., and Gibo, D.M. (2005). Fos-related antigen 1 modulates malignant
903 features of glioma cells. *Mol. Cancer Res.* *3*, 237–249.
- 904 Diesch, J., Sanij, E., Gilan, O., Love, C., Tran, H., Fleming, N.I., Ellul, J., Amalia, M.,
905 Haviv, I., Pearson, R.B., et al. (2014). Widespread FRA1-Dependent Control of
906 Mesenchymal Transdifferentiation Programs in Colorectal Cancer Cells. *PLoS One* *9*,
907 1–11.
- 908 Dobin, A., Davis, C.A., Schlesinger, F., Drenkow, J., Zaleski, C., Jha, S., Batut, P.,
909 Chaisson, M., and Gingeras, T.R. (2013). STAR: ultrafast universal RNA-seq aligner.
910 *Bioinformatics* *29*, 15–21.
- 911 Eferl, R., and Wagner, E.F. (2003). AP-1: A double-edged sword in tumorigenesis. *Nat.*
912 *Rev. Cancer* *3*, 859–868.
- 913 Fedele, M., Cerchia, L., Pegoraro, S., Sgarra, R., and Manfioletti, G. (2019). Proneural-
914 Mesenchymal Transition: Phenotypic Plasticity to Acquire Multitherapy Resistance in
915 Glioblastoma. *Int. J. Mol. Sci.* *20*, 2746.
- 916 Fedele, V., Dai, F., Masilamani, A.P., Heiland, D.H., Kling, E., Gätjens-Sanchez, A.M.,
917 Ferrarese, R., Platania, L., Soroush, D., Kim, H., et al. (2017). Epigenetic Regulation of
918 ZBTB18 Promotes Glioblastoma Progression. *Mol. Cancer Res.* *15*, 998–1011.
- 919 Fletcher, M.N.C., Castro, M.A.A., Wang, X., de Santiago, I., O’Reilly, M., Chin, S.-F.,
920 Rueda, O.M., Caldas, C., Ponder, B.A.J., Markowitz, F., et al. (2013). Master regulators
921 of FGFR2 signalling and breast cancer risk. *Nat. Commun.* *4*, 2464.
- 922 Friedmann-Morvinski, D., Bushong, E.A., Ke, E., Soda, Y., Marumoto, T., Singer, O.,
923 Ellisman, M.H., and Verma, I.M. (2012). Dedifferentiation of neurons and astrocytes by

- 924 oncogenes can induce gliomas in mice. *Science* 338, 1080–1084.
- 925 Gao, X.-Q., Ge, Y.-S., Shu, Q.-H., and Ma, H.-X. (2017). Expression of Fra-1 in human
926 hepatocellular carcinoma and its prognostic significance. *Tumour Biol.* 39,
927 1010428317709635.
- 928 Günther, H.S., Schmidt, N.O., Phillips, H.S., Kemming, D., Kharbanda, S., Soriano, R.,
929 Modrusan, Z., Meissner, H., Westphal, M., and Lamszus, K. (2008). Glioblastoma-
930 derived stem cell-enriched cultures form distinct subgroups according to molecular and
931 phenotypic criteria. *Oncogene* 27, 2897–2909.
- 932 Halliday, J., Helmy, K., Pattwell, S.S., Pitter, K.L., LaPlant, Q., Ozawa, T., and
933 Holland, E.C. (2014). In vivo radiation response of proneural glioma characterized by
934 protective p53 transcriptional program and proneural-mesenchymal shift. *Proc. Natl.*
935 *Acad. Sci.* 111, 5248–5253.
- 936 Hambardzumyan, D., Amankulor, N.M., Helmy, K.Y., Becher, O.J., and Holland, E.C.
937 (2009). Modeling Adult Gliomas Using RCAS/t-va Technology. *Transl. Oncol.* 2, 89–
938 95.
- 939 Hasenfuss, S.C., Bakiri, L., Thomsen, M.K., Hamacher, R., and Wagner, E.F. (2014).
940 Activator protein 1 transcription factor fos-related antigen 1 (fra-1) is dispensable for
941 murine liver fibrosis, but modulates xenobiotic metabolism. *Hepatology* 59, 261–273.
- 942 Holland, E.C., Celestino, J., Dai, C., Schaefer, L., Sawaya, R.E., and Fuller, G.N.
943 (2000). Combined activation of Ras and Akt in neural progenitors induces glioblastoma
944 formation in mice. *Nat. Genet.* 25, 55–57.
- 945 Koschmann, C., Calinescu, A.-A., Nunez, F.J., Mackay, A., Fazal-Salom, J., Thomas,
946 D., Mendez, F., Kamran, N., Dzaman, M., Mulpuri, L., et al. (2016). ATRX loss
947 promotes tumor growth and impairs nonhomologous end joining DNA repair in glioma.
948 *Sci. Transl. Med.* 8, 328ra28.
- 949 Lau, E.Y.T., Lo, J., Cheng, B.Y.L., Ma, M.K.F., Lee, J.M.F., Ng, J.K.Y., Chai, S., Lin,
950 C.H., Tsang, S.Y., Ma, S., et al. (2016). Cancer-Associated Fibroblasts Regulate
951 Tumor-Initiating Cell Plasticity in Hepatocellular Carcinoma through c-
952 Met/FRA1/HEY1 Signaling. *Cell Rep.* 15, 1175–1189.

- 953 Liu, H., Ren, G., Wang, T., Chen, Y., Gong, C., Bai, Y., Wang, B., Qi, H., Shen, J.,
954 Zhu, L., et al. (2015). Aberrantly expressed Fra-1 by IL-6/STAT3 transactivation
955 promotes colorectal cancer aggressiveness through epithelial-mesenchymal transition.
956 *Carcinogenesis* *36*, 459–468.
- 957 Love, M.I., Huber, W., and Anders, S. (2014). Moderated estimation of fold change and
958 dispersion for RNA-seq data with DESeq2. *Genome Biol.* *15*, 550.
- 959 Mack, S.C., Singh, I., Wang, X., Hirsch, R., Wu, Q., Villagomez, R., Bernatchez, J.A.,
960 Zhu, Z., Gimble, R.C., Kim, L.J.Y., et al. (2019). Chromatin landscapes reveal
961 developmentally encoded transcriptional states that define human glioblastoma. *J. Exp.*
962 *Med.* *216*, 1071–1090.
- 963 Mani, S.A., Guo, W., Liao, M.-J., Eaton, E.N., Ayyanan, A., Zhou, A.Y., Brooks, M.,
964 Reinhard, F., Zhang, C.C., Shipitsin, M., et al. (2008). The epithelial-mesenchymal
965 transition generates cells with properties of stem cells. *Cell* *133*, 704–715.
- 966 Mansuy, I.M., and Bujard, H. (2000). Tetracycline-regulated gene expression in the
967 brain. *Curr. Opin. Neurobiol.* *10*, 593–596.
- 968 Mao, P., Joshi, K., Li, J., Kim, S.-H., Li, P., Santana-Santos, L., Luthra, S., Chandran,
969 U.R., Benos, P. V., Smith, L., et al. (2013). Mesenchymal glioma stem cells are
970 maintained by activated glycolytic metabolism involving aldehyde dehydrogenase 1A3.
971 *Proc. Natl. Acad. Sci.* *110*, 8644–8649.
- 972 McCormick, F. (1990). GAP as ras effector or negative regulator? *Mol. Carcinog.* *3*,
973 185–187.
- 974 Muñoz, D.M., Tung, T., Agnihotri, S., Singh, S., Guha, A., Zadeh, G., and Hawkins, C.
975 (2013). Loss of p53 cooperates with K-ras activation to induce glioma formation in a
976 region-independent manner. *Glia* *61*, 1862–1872.
- 977 Neftel, C., Laffy, J., Filbin, M.G., Hara, T., Shore, M.E., Rahme, G.J., Richman, A.R.,
978 Silverbush, D., Shaw, M.L., Hebert, C.M., et al. (2019). An Integrative Model of
979 Cellular States, Plasticity, and Genetics for Glioblastoma. *Cell* *178*, 835-849.e21.
- 980 Oldrini, B., Curiel-García, Á., Marques, C., Matia, V., Uluçkan, Ö., Graña-Castro, O.,
981 Torres-Ruiz, R., Rodriguez-Perales, S., Huse, J.T., and Squatrito, M. (2018). Somatic

- 982 genome editing with the RCAS-TVA-CRISPR-Cas9 system for precision tumor
983 modeling. *Nat. Commun.* *9*, 1466.
- 984 Ozawa, T., Riestler, M., Cheng, Y.K., Huse, J.T., Squatrito, M., Helmy, K., Charles, N.,
985 Michor, F., and Holland, E.C. (2014). Most human non-GCIMP glioblastoma subtypes
986 evolve from a common proneural-like precursor glioma. *Cancer Cell* *26*, 288–300.
- 987 Patel, A.P., Tirosh, I., Trombetta, J.J., Shalek, A.K., Gillespie, S.M., Wakimoto, H.,
988 Cahill, D.P., Nahed, B. V, Curry, W.T., Martuza, R.L., et al. (2014). Single-cell RNA-
989 seq highlights intratumoral heterogeneity in primary glioblastoma. *Science* *344*, 1396–
990 1401.
- 991 Phillips, H.S., Kharbanda, S., Chen, R., Forrester, W.F., Soriano, R.H., Wu, T.D., Misra,
992 A., Nigro, J.M., Colman, H., Soroceanu, L., et al. (2006). Molecular subclasses of high-
993 grade glioma predict prognosis, delineate a pattern of disease progression, and resemble
994 stages in neurogenesis. *Cancer Cell* *9*, 157–173.
- 995 Ricci-Vitiani, L., Pallini, R., Larocca, L.M., Lombardi, D.G., Signore, M., Pierconti, F.,
996 Petrucci, G., Montano, N., Maira, G., and De Maria, R. (2008). Mesenchymal
997 differentiation of glioblastoma stem cells. *Cell Death Differ.* *15*, 1491–1498.
- 998 Sandberg, C.J., Altschuler, G., Jeong, J., Strømme, K.K., Stangeland, B., Murrell, W.,
999 Grasmø-Wendler, U.H., Myklebost, O., Helseth, E., Vik-Mo, E.O., et al. (2013).
1000 Comparison of glioma stem cells to neural stem cells from the adult human brain
1001 identifies dysregulated Wnt- signaling and a fingerprint associated with clinical
1002 outcome. *Exp. Cell Res.* *319*, 2230–2243.
- 1003 Sottoriva, A., Spiteri, I., Piccirillo, S.G.M., Touloumis, A., Collins, V.P., Marioni, J.C.,
1004 Curtis, C., Watts, C., and Tavare, S. (2013). Intratumor heterogeneity in human
1005 glioblastoma reflects cancer evolutionary dynamics. *Proc. Natl. Acad. Sci.* *110*, 4009–
1006 4014.
- 1007 Subramanian, A., Tamayo, P., Mootha, V.K., Mukherjee, S., Ebert, B.L., Gillette, M.A.,
1008 Paulovich, A., Pomeroy, S.L., Golub, T.R., Lander, E.S., et al. (2005). Gene set
1009 enrichment analysis: a knowledge-based approach for interpreting genome-wide
1010 expression profiles. *Proc. Natl. Acad. Sci. U. S. A.* *102*, 15545–15550.
- 1011 Tam, W.L., and Weinberg, R.A. (2013). The epigenetics of epithelial-mesenchymal

- 1012 plasticity in cancer. *Nat. Med.* *19*, 1438–1449.
- 1013 Tam, W.L., Lu, H., Buikhuisen, J., Soh, B.S., Lim, E., Reinhardt, F., Wu, Z.J., Krall,
1014 J.A., Bieri, B., Guo, W., et al. (2013). Protein kinase C alpha is a central signaling
1015 node and therapeutic target for breast cancer stem cells. *Cancer Cell* *24*, 347–364.
- 1016 The Cancer Genome Atlas Research Network (2008). Comprehensive genomic
1017 characterization defines human glioblastoma genes and core pathways. *Nature* *455*,
1018 1061–1068.
- 1019 Tso, C.-L., Shintaku, P., Chen, J., Liu, Q., Liu, J., Chen, Z., Yoshimoto, K., Mischel,
1020 P.S., Cloughesy, T.F., Liao, L.M., et al. (2006). Primary Glioblastomas Express
1021 Mesenchymal Stem-Like Properties. *Mol. Cancer Res.* *4*, 607–619.
- 1022 Uhrbom, L., Dai, C., Celestino, J.C., Rosenblum, M.K., Fuller, G.N., and Holland, E.C.
1023 (2002). Ink4a-Arf loss cooperates with KRas activation in astrocytes and neural
1024 progenitors to generate glioblastomas of various morphologies depending on activated
1025 Akt. *Cancer Res.* *62*, 5551–5558.
- 1026 Usui, A., Hoshino, I., Akutsu, Y., Sakata, H., Nishimori, T., Murakami, K., Kano, M.,
1027 Shuto, K., and Matsubara, H. (2012). The molecular role of Fra-1 and its prognostic
1028 significance in human esophageal squamous cell carcinoma. *Cancer* *118*, 3387–3396.
- 1029 Vallejo, A., Perurena, N., Guruceaga, E., Mazur, P.K., Martinez-Canarias, S., Zandueta,
1030 C., Valencia, K., Arricibita, A., Gwinn, D., Sayles, L.C., et al. (2017). An integrative
1031 approach unveils FOSL1 as an oncogene vulnerability in KRAS-driven lung and
1032 pancreatic cancer. *Nat. Commun.* *8*.
- 1033 Verde, P., Casalino, L., Talotta, F., Yaniv, M., and Weitzman, J.B. (2007). Deciphering
1034 AP-1 function in tumorigenesis: fra-ternizing on target promoters. *Cell Cycle* *6*, 2633–
1035 2639.
- 1036 Verhaak, R.G.W., Hoadley, K.A., Purdom, E., Wang, V., Qi, Y., Wilkerson, M.D.,
1037 Miller, C.R., Ding, L., Golub, T., Mesirov, J.P., et al. (2010). Integrated Genomic
1038 Analysis Identifies Clinically Relevant Subtypes of Glioblastoma Characterized by
1039 Abnormalities in PDGFRA, IDH1, EGFR, and NF1. *Cancer Cell* *17*, 98–110.
- 1040 Wang, J., Cazzato, E., Ladewig, E., Frattini, V., Rosenbloom, D.I.S., Zairis, S., Abate,

- 1041 F., Liu, Z., Elliott, O., Shin, Y.-J., et al. (2016). Clonal evolution of glioblastoma under
1042 therapy. *Nat. Genet.* *48*, 768–776.
- 1043 Wang, L., Babikir, H., Muller, S., Yagnik, G., Shamardani, K., Catalan, F., Kohanbash,
1044 G., Alvarado, B., Di Lullo, E., Kriegstein, A., et al. (2019). The phenotypes of
1045 proliferating glioblastoma cells reside on a single axis of variation. *Cancer Discov.* CD-
1046 19-0329.
- 1047 Wang, Q., Hu, B., Hu, X., Kim, H., Squatrito, M., Scarpace, L., deCarvalho, A.C., Lyu,
1048 S., Li, P., Li, Y., et al. (2017). Tumor Evolution of Glioma-Intrinsic Gene Expression
1049 Subtypes Associates with Immunological Changes in the Microenvironment. *Cancer*
1050 *Cell* *32*, 42-56.e6.
- 1051 Wu, J., Ji, A., Wang, X., Zhu, Y., Yu, Y., Lin, Y., Liu, Y., Li, S., Liang, Z., Xu, X., et
1052 al. (2015). MicroRNA-195-5p, a new regulator of Fra-1, suppresses the migration and
1053 invasion of prostate cancer cells. *J. Transl. Med.* *13*, 289.
- 1054 Xu, H., Jin, X., Yuan, Y., Deng, P., Jiang, L., Zeng, X., Li, X.-S., Wang, Z.-Y., and
1055 Chen, Q.-M. (2017). Prognostic value from integrative analysis of transcription factors
1056 c-Jun and Fra-1 in oral squamous cell carcinoma: a multicenter cohort study. *Sci. Rep.*
1057 *7*, 7522.
- 1058 Ye, X., Tam, W.L., Shibue, T., Kaygusuz, Y., Reinhardt, F., Ng Eaton, E., and
1059 Weinberg, R.A. (2015). Distinct EMT programs control normal mammary stem cells
1060 and tumour-initiating cells. *Nature* *525*, 256–260.
- 1061
- 1062

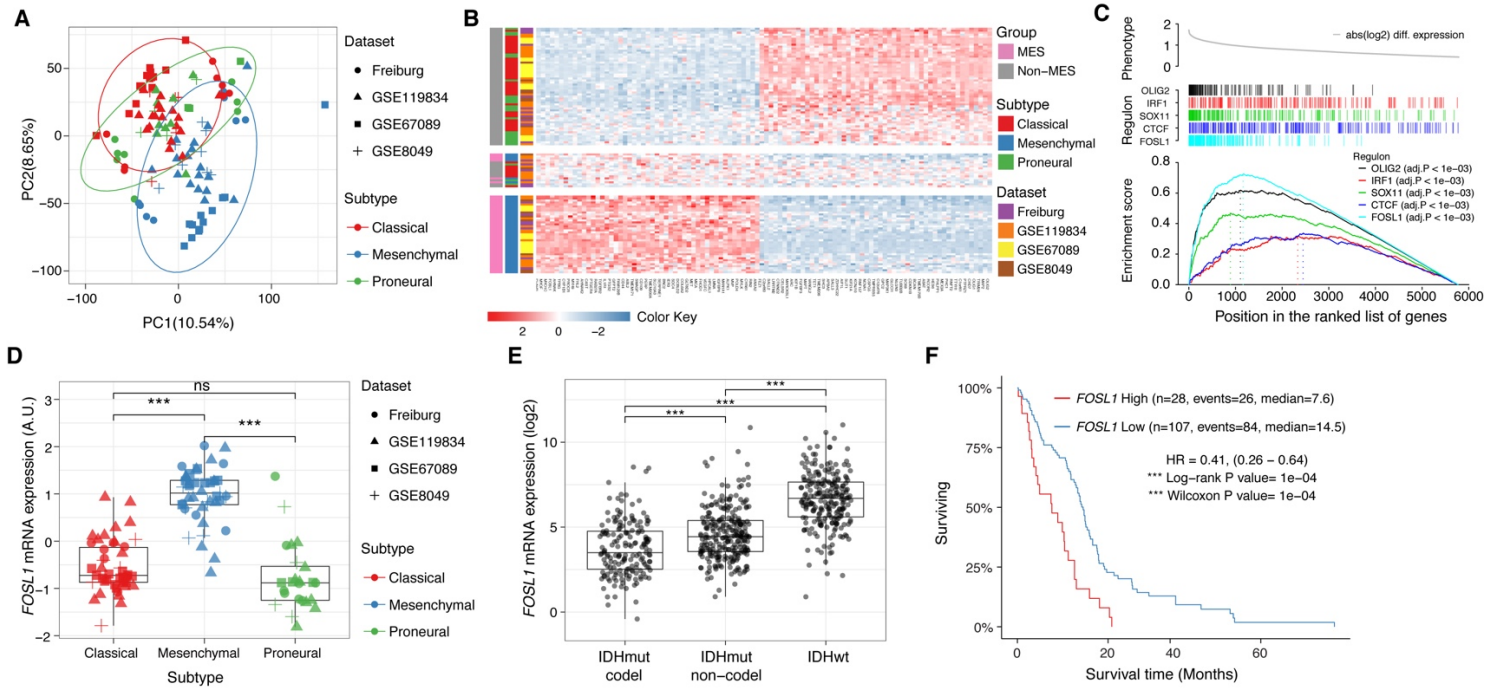


Figure 1. *FOSL1* is a master regulator of the glioma-intrinsic MES transcriptional signature. **A)** Principal Component (PC) analysis of the BTSCs expression dataset. **B)** Heatmap of the top 100 differentially expressed genes between MES and Non-MES BTSCs. **C)** One-tail GSEA of the top 5 scoring TFs in the MRA. **D)** *FOSL1* mRNA expression in the BTSCs dataset. Student's t test, * $P \leq 0.05$, *** $P \leq 0.001$. **E)** *FOSL1* mRNA expression in the TCGA dataset. Tumors were separated according to their molecular subtype classification. Student's t test, *** $P \leq 0.001$. **F)** Kaplan-Meier survival curves of the IDH-wt GBM TCGA tumors stratified based on *FOSL1* expression. See also Figure S1.

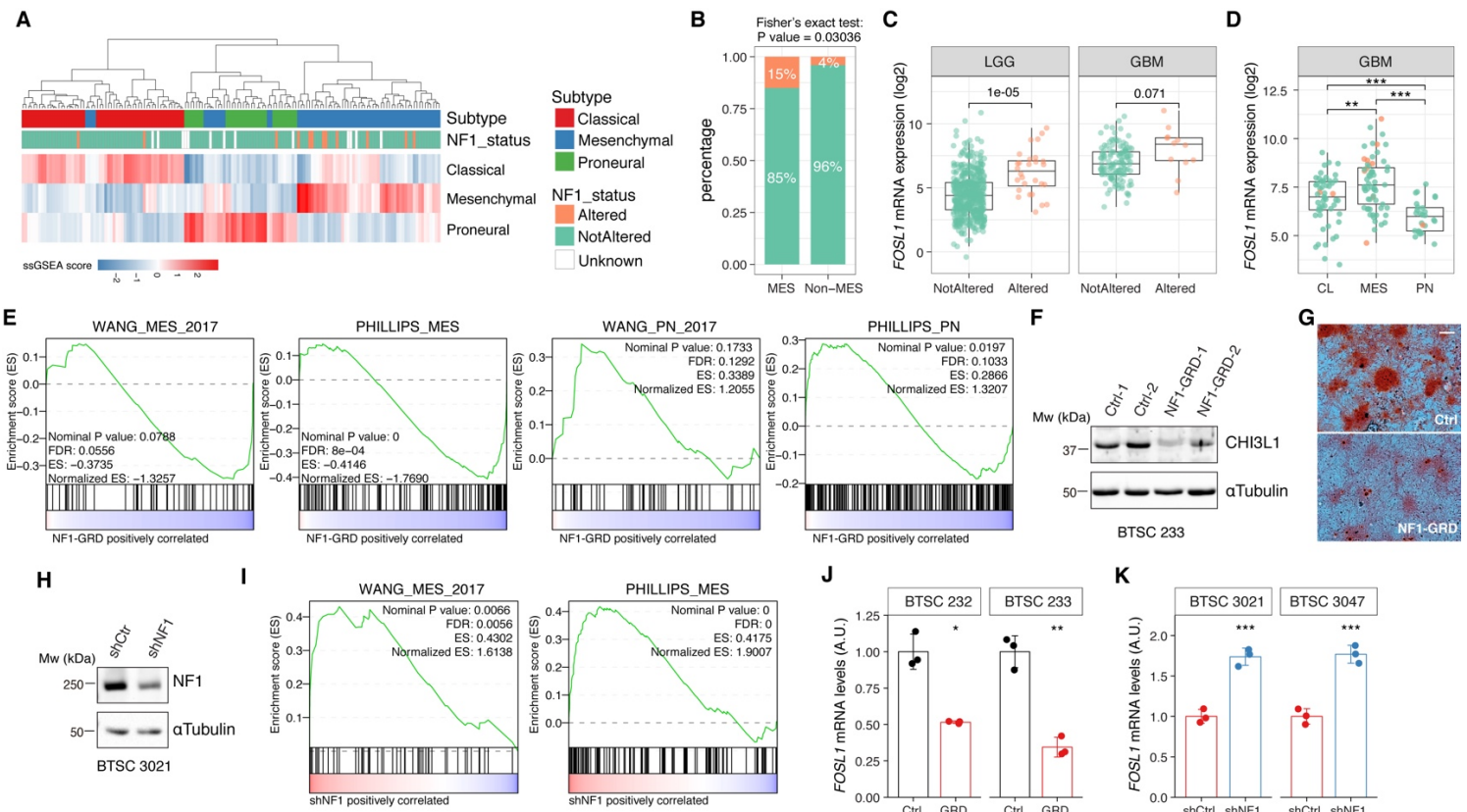


Figure 2. *NF1* is a functional modulator of MES transcriptional signature and *FOSL1* expression. **A)** Heatmap of the subtype ssGSEA scores and *NF1* genetic alterations of the IDH-wt GBM TCGA tumors. **B)** Frequency of *NF1* alterations in MES and Non-MES GBMs. Colors are as in panel A. **C)** and **D)** *FOSL1* mRNA expression in the TCGA dataset. Tumors were separated according to either *NF1* alterations (C) or transcriptional subtypes (D). Colors are as in panel A. Student's t test, ** $P \leq 0.01$, *** $P \leq 0.001$. **E)** GSEA of BTSC 233 MES cells transduced with *NF1*-GRD expressing lentivirus versus Ctrl. Gene signatures from Wang and Phillips studies were analyzed (MES, *left panels*; PN, *right panels*). ES = Enrichment score. **F)** Western blot analysis of whole-cell-extract of BTSC 233 cells showing CHI3L1 mesenchymal marker expression upon *NF1*-GRD transduction. Tubulin was used as loading control. **G)** Osteogenesis differentiation assay of BTSC 233 transduced as indicated above. Alizarin Red staining indicates osteogenesis differentiation. Scale bar represents 200 μm . **H)** Western blot analysis of whole-cell-extract of proneural BTSC 3021 cells transduced with either *NF1* (sh*NF1*) or control (shCtrl) shRNAs. **I)** GSEA of BTSC 3021 transduced with sh*NF1* versus Ctrl. **J)** and **K)** qRT-PCR analysis of *FOSL1* expression upon *NF1*-GRD overexpression in BTSC 232 and BTSC 233 cells (J) or *NF1* knockdown in 3021 and 3047 cells (K). Data are presented as mean \pm SD (n=3), normalized to 18s rRNA expression; Student's t test, * $P \leq 0.05$, ** $P \leq 0.01$, *** $P \leq 0.001$. See also Figure S2-S3.

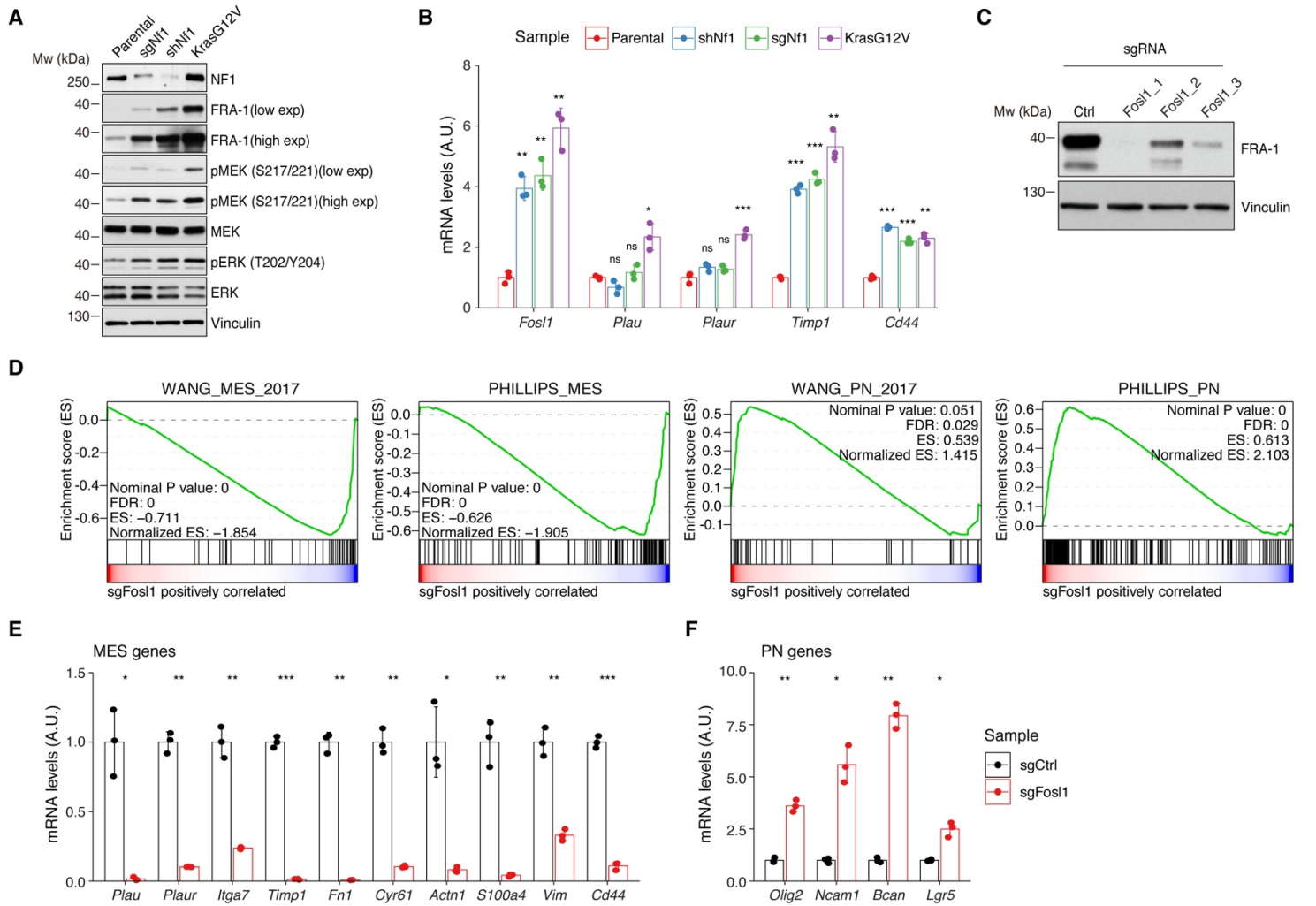


Figure 3. *Fosl1* is induced by MAPK kinase activation and is required for MES gene expression. A) Western blot analysis using the specified antibodies of p53-null NSCs, parental and infected with *sgNf1*, *shNf1* and *Kras^{G12V}*; Vinculin used as loading control. **B)** mRNA expression of *Fosl1* and MES genes (*Plau*, *Plaur*, *Timp1* and *Cd44*), in infected p53-null NSCs, compared to parental cells (not infected). Data from a representative of two experiments are presented as mean \pm SD (n=3), normalized to *Gapdh* expression. Student's t test, relative to parental cells: ns = not significant, * $P < 0.05$, ** $P < 0.01$, *** $P < 0.001$. **C)** FRA-1 expression detected by Western blot in p53-null *Kras^{G12V}* NSCs upon transduction with sgRNAs targeting *Fosl1*, after selection with 1 μ g/mL puromycin; Vinculin used as loading control. **D)** GSEA of p53-null *Kras^{G12V}* *sgFosl1_1* versus *sgCtrl* NSCs. Gene signatures from Wang and Phillips studies were analyzed (MES, left panels; PN, right panels). **E)** and **F)** mRNA expression of MES and PN genes, respectively, in *sgCtrl* and *sgFosl1_1* p53-null *Kras^{G12V}* NSCs. Data from a representative of two experiments are presented as mean \pm SD (n=3), normalized to *Gapdh* expression. Student's t test, relative to *sgCtrl*: * $P < 0.05$; ** $P < 0.01$; *** $P < 0.001$.

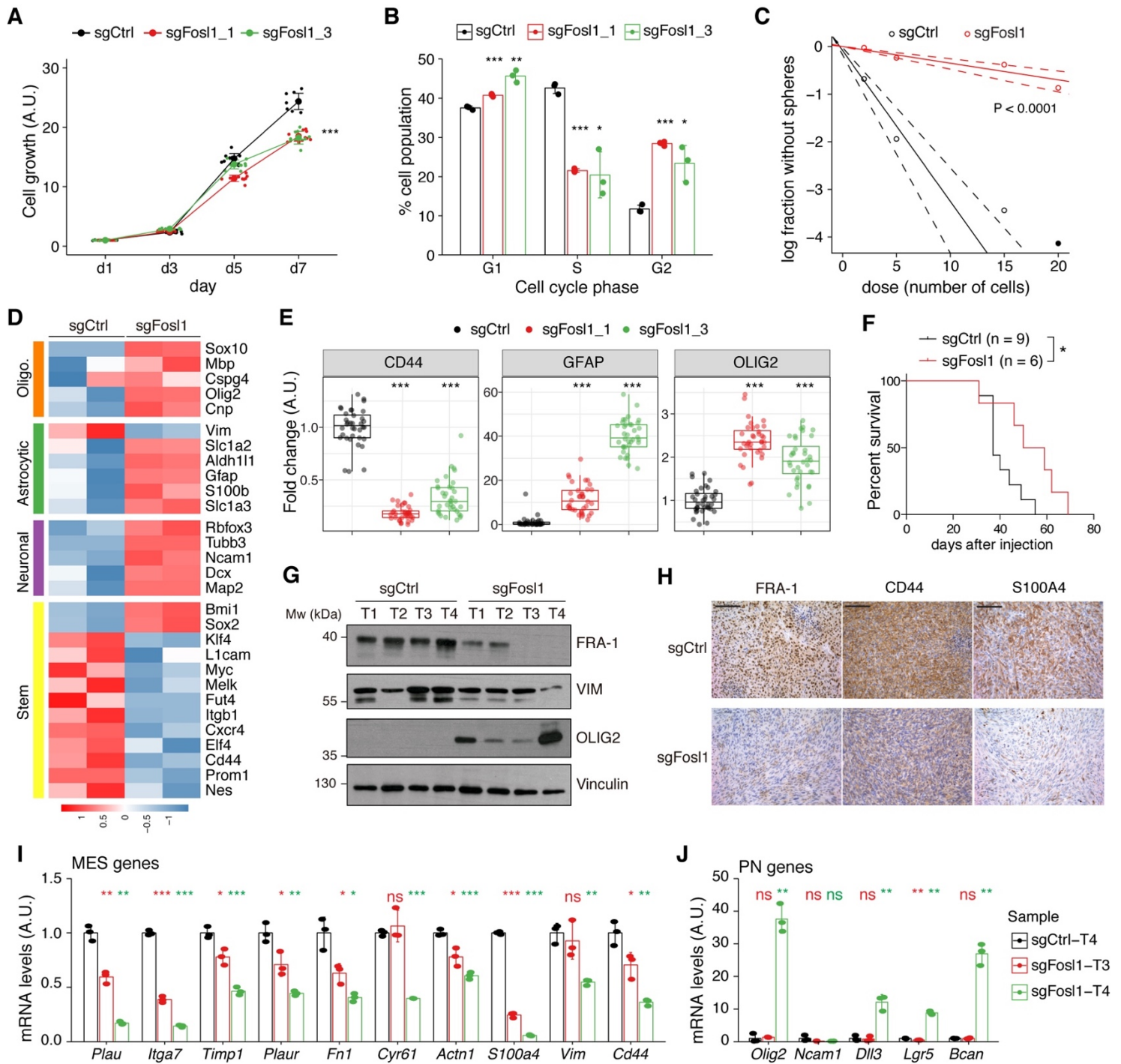


Figure 4. *Fos11* knock-out impairs cell growth and stemness *in vitro* and increases survival in a xenograft model. **A)** Cell viability of control and *Fos11* KO p53-null *Kras*^{G12V} NSCs measured by MTT assay; absorbance values were normalized to day 1. Data from a representative of three independent experiments are presented as mean \pm SD (n=10). Student's t test on day 7, relative to sgCtrl: *** $P \leq 0.001$. **B)** Quantification of cell cycle populations of control and *Fos11* KO p53-null *Kras*^{G12V} NSCs by flow cytometry analysis of PI staining. Data from a representative of two independent experiments are presented as mean \pm SD (n=3). Student's t test, relative to sgCtrl: * $P \leq 0.05$; ** $P \leq 0.01$; *** $P \leq 0.001$. **C)** A representative limiting dilution experiment on p53-null *Kras*^{G12V} sgCtrl and sg*Fos11_1* NSCs, calculated with extreme limiting dilution assay (ELDA) analysis; $P < 0.0001$. **D)** Heatmap of expression of stem cell (yellow) and lineage-specific (neuronal – purple, astrocytic – green and oligodendrocytic – orange) genes, comparing sgCtrl and sg*Fos11_1* p53-null *Kras*^{G12V} NSCs. **E)** Quantification of pixel area (fold change)

relative to sgCtrl) of CD44, GFAP and OLIG2 relative to DAPI pixel area per field of view in control and *Fosll* KO p53-null *Kras*^{G12V} NSCs. Data from a representative of two independent experiments; Student's t test, relative to sgCtrl: ***P ≤ 0.001. **F**) Kaplan-Meier survival curves of *nu/nu* mice injected with p53-null *Kras*^{G12V} sgCtrl (n=9) and sg*Fosll*_1 (n=6) NSCs. Log-rank P = 0.0263. **G**) Western blot analysis using the indicated antibodies of 4 sgCtrl and 4 sg*Fosll*_1 tumors (showing low or no detectable expression of FRA-1); Vinculin used as loading control. **H**) Representative images of IHCs using the indicated antibodies. Scale bars represent 100 μm. **I**) mRNA expression of MES genes in the samples sgCtrl-T4 (higher FRA-1 expression) and sg*Fosll*_1-T3 and -T4 (no detectable FRA-1 expression). **J**) mRNA expression of PN genes in samples as in (H). Data from a representative of two experiments are presented as mean ± SD (n=3), normalized to *Gapdh* expression. Student's t test for sg*Fosll*_1 tumors, relative to sgCtrl-T4: ns = not significant, *P ≤ 0.05, **P ≤ 0.01, ***P ≤ 0.001. See also Figure S4.

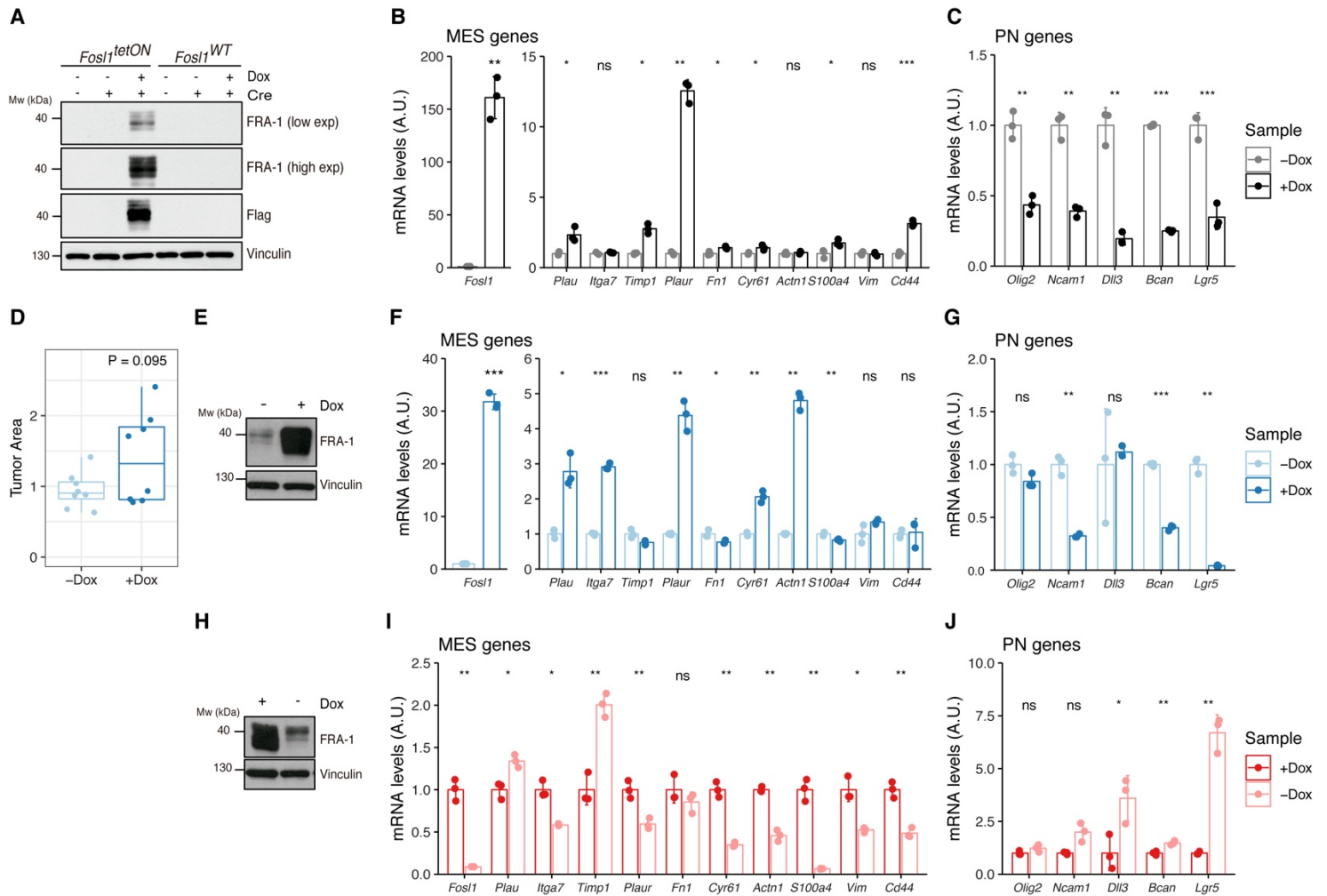


Figure 5. *Fos11* overexpression upregulates the MGS and induces larger tumors *in vivo*. **A)** Western blot analysis of FRA-1 and Flag expression on *Fos11*^{tetON} and *Fos11*^{WT} NCS derived from *Kras*^{LSLG12V}; *Trp53*^{lox}; *ROSA26*^{LSLrtTA-IRES-EGFP}; *Colla1*^{TetO-Fos11} mice, upon *in vitro* infection with Cre and induction of *Fos11* overexpression with 1 μg/mL Dox for 72 h; Vinculin used as loading control. **B)** mRNA expression of *Fos11* and MES genes in *Fos11*^{tetON} p53-null *Kras*^{G12V} cells upon 72 h induction with 1 μg/mL Dox. **C)** mRNA expression of PN genes in *Fos11*^{tetON} p53-null *Kras*^{G12V} cells upon 72 h induction with 1 μg/mL Dox. **D)** Quantification of tumor area (μm²) of -Dox and +Dox tumors (n=8/8). For each mouse, the brain section on the H&E slide with a larger tumor was considered and quantified using the ZEN software (Zeiss). **E)** Western blot detection of FRA-1 expression in tumorspheres derived from a control (-Dox) tumor. Tumorspheres were isolated and kept without Dox until first passage, when 1 μg/mL Dox was added and kept for 19 days (+Dox *in vitro*). **F)** mRNA expression of *Fos11* and MES genes in tumorspheres in absence or presence of Dox for 19 days. **G)** mRNA expression of PN genes in tumorspheres in absence or presence of Dox for 19 days. **H)** Western blot detection of FRA-1 expression in tumorspheres derived from a *Fos11* overexpressing (+Dox) tumor. Tumorspheres were isolated and kept with 1 μg/mL Dox until first passage, when Dox was removed for 19 days (-Dox *in vitro*). **I)** mRNA expression of *Fos11* and MES genes in tumorspheres in presence or absence of Dox for 19 days. **J)** mRNA expression of PN genes in tumorspheres in presence or absence of Dox for 19 days. qPCR data from a representative of two experiments are presented as mean ± SD (n=3), normalized to *Gapdh* expression. Student's t test, relative to the respective control (-Dox in B, C, F and G; +Dox in I and J): ns = not significant, *P ≤ 0.05, **P ≤ 0.01, ***P ≤ 0.001. See also Figure S5.

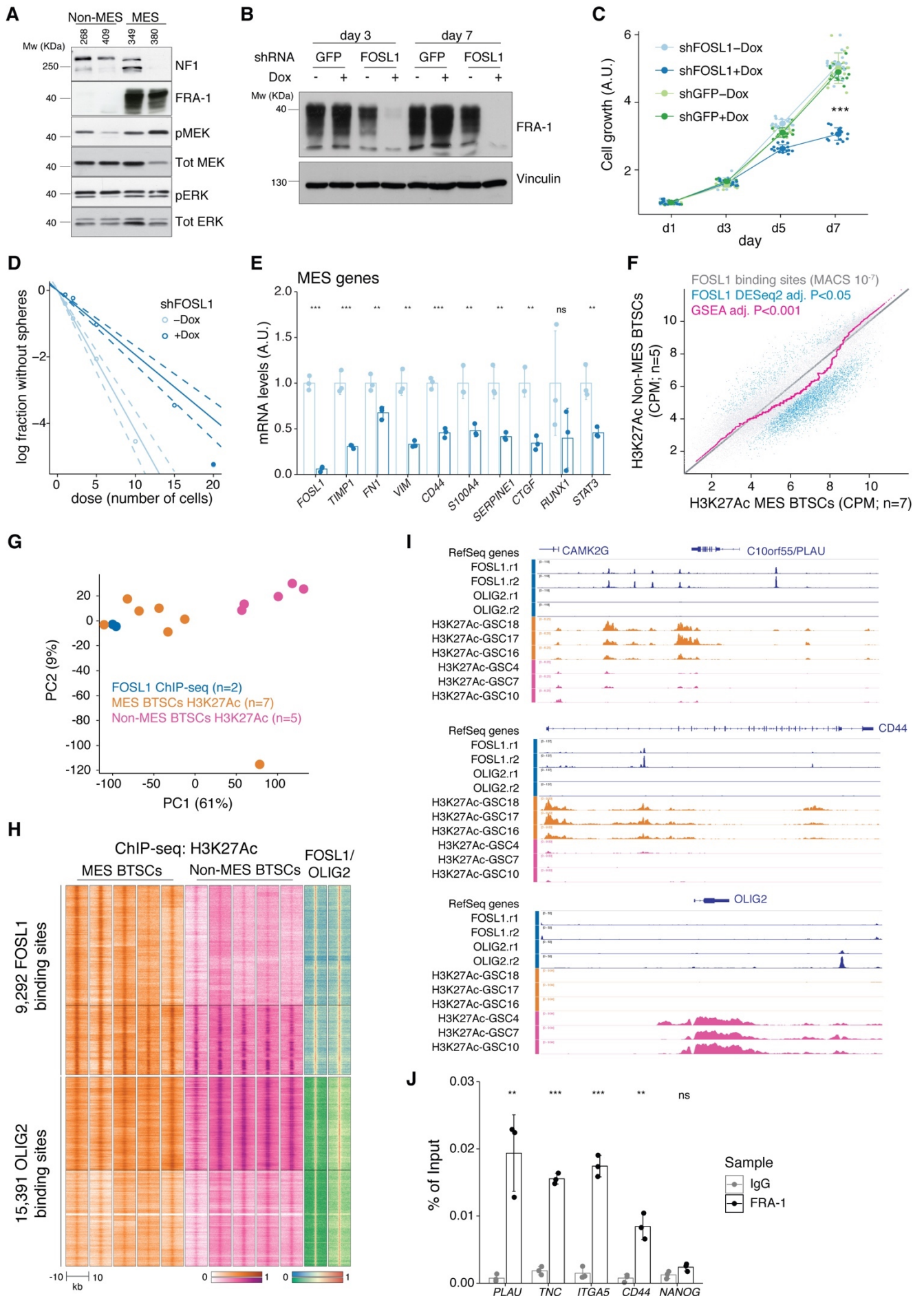
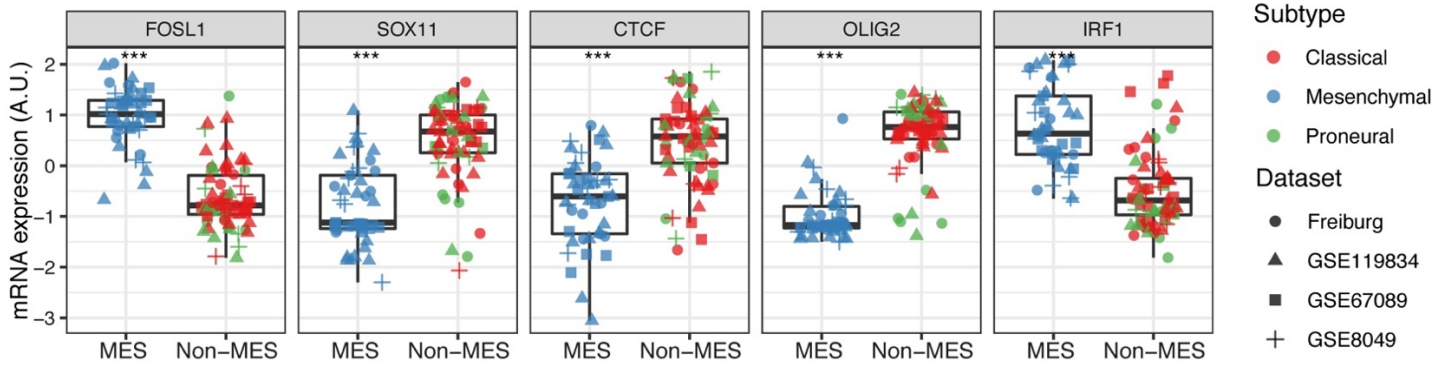


Figure 6. *FOSL1* silencing in a patient-derived MES tumor stem cell line decreases cell growth, stemness and MGS *in vitro*. **A)** Western blot analysis using the specified antibodies of human brain tumor stem cell lines, characterized as Non-MES (*left*) and MES (*right*). **B)** Western blot detection of FRA-1 in MES BTSC 349 upon transduction with inducible shRNAs targeting GFP (control) and *FOSL1*, analyzed after 3 and 7 days of Dox treatment; Vinculin used as loading control. **C)** Cell growth of BTSC 349 shGFP and sh*FOSL1*, in absence or presence of Dox, measured by MTT assay; absorbance values were normalized to day 1. Data from a representative of three independent experiments are presented as mean \pm SD (n=15). Student's t test on day 7, relative to sh*FOSL1* –Dox: ***P \leq 0.001. **D)** Representative limiting dilution analysis on BTSC 349 sh*FOSL1*, in presence or absence of Dox, calculated with extreme limiting dilution assay (ELDA) analysis; P < 0.0001. **E)** mRNA expression of *FOSL1* and MES genes in BTSC 349 sh*FOSL1* in absence or presence of Dox for 3 days. Data from a representative of three experiments are presented as mean \pm SD (n=3), normalized to *GAPDH* expression. Student's t test, relative to –Dox: ns = not significant, *P \leq 0.05, **P \leq 0.01, ***P \leq 0.001. **F)** Scatter plot of H3K27Ac signal for Non-Mes and MES BTSCs (from Mack et al., 2019) on *FOSL1*/FRA-1 peaks calculated using MACS on ENCODE samples (see methods). Blue probes represent statistically significant difference in H3K27Ac signal between Non-Mes and MES BTSCs. Violet trendline indicates a custom regression calculated by a Kolmogorov-Smirnov test, adj-P < 0.05, z > 0.5. **G)** Principal component analysis of H3K27Ac of *FOSL1*/FRA-1 enrichment over *FOSL1*/FRA-1 binding sites for the indicated samples. **H)** Heatmap of ChIP-seq enrichment of *FOSL1*/FRA-1 or OLIG2 binding sites for the indicated profiles. **I)** IGV browser view of the *PLAU*, *CD44* and *OLIG2* loci of selected profiles. **J)** Representative ChIP experiment in BTSC 349 cells. The panel shows FRA-1 binding to the promoter of a subset of mesenchymal targets (n=3 PCR replicates) expressed as percentage of the initial DNA amount in the immune-precipitated fraction. *NANOG* gene was used as a negative control. Student's t test, relative to IgG: ns = not significant, **P \leq 0.01, ***P \leq 0.001. See also Figure S6.

A



B

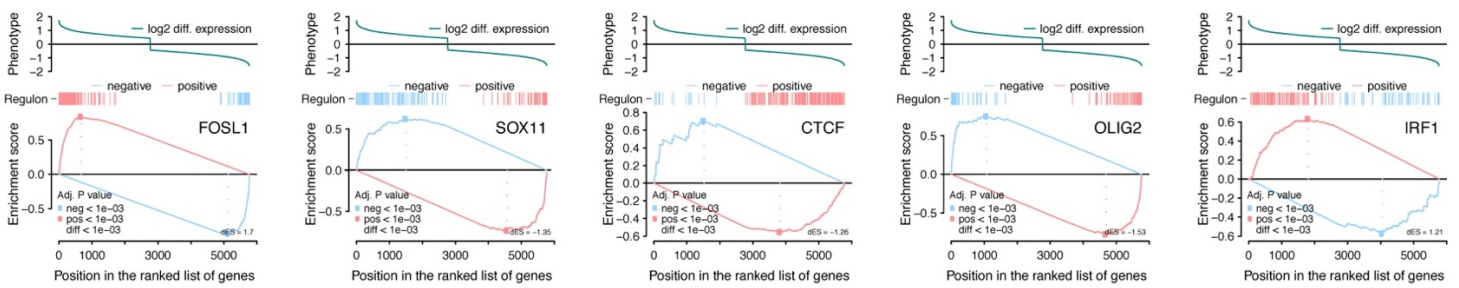
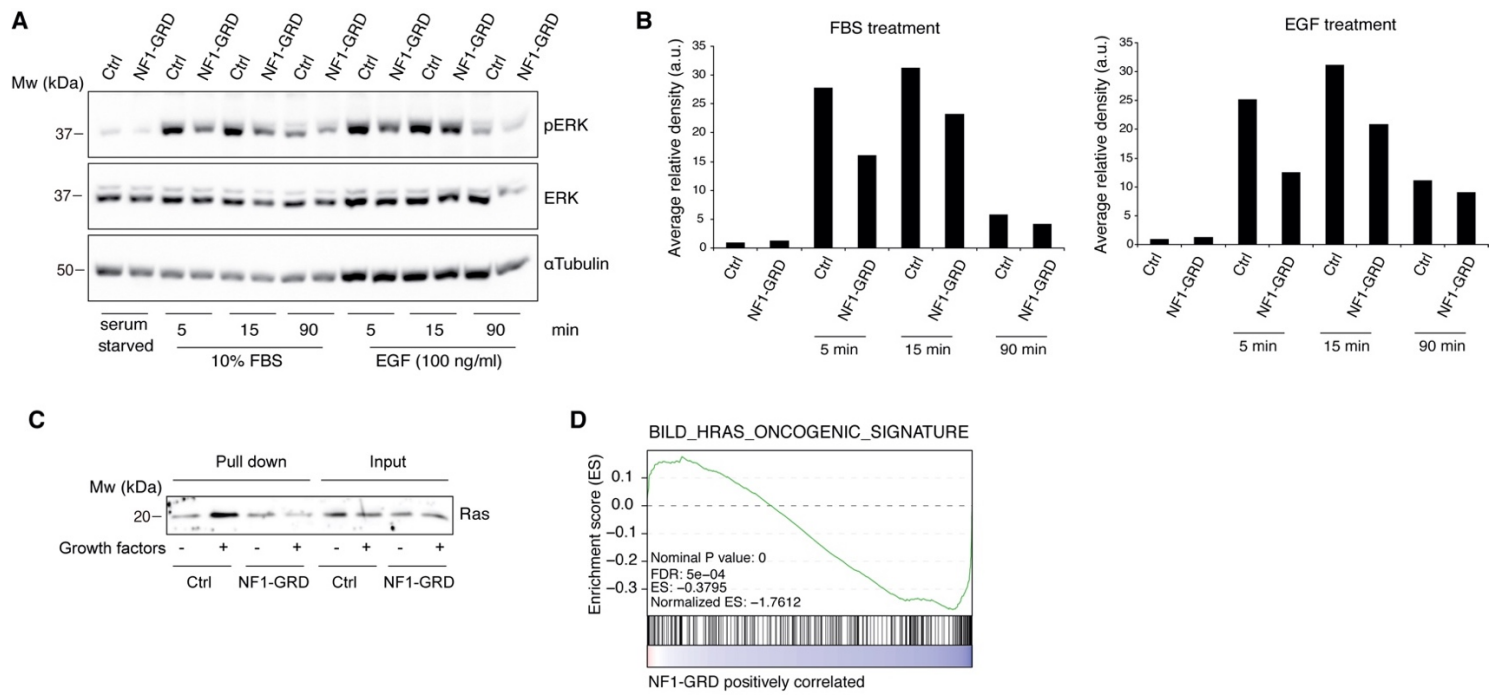


Figure S1. Related to Figure 1. A) mRNA expression of the top 5 scoring TFs in the MRA of the BTSCs dataset, comparing MES versus Non-MES. Student's t test, ***P < 0.001. **B)** Two-tailed GSEA showing positive or negative targets for the top 5 TFs in the MRA ranked by their differential expression (MES vs Non-MES).



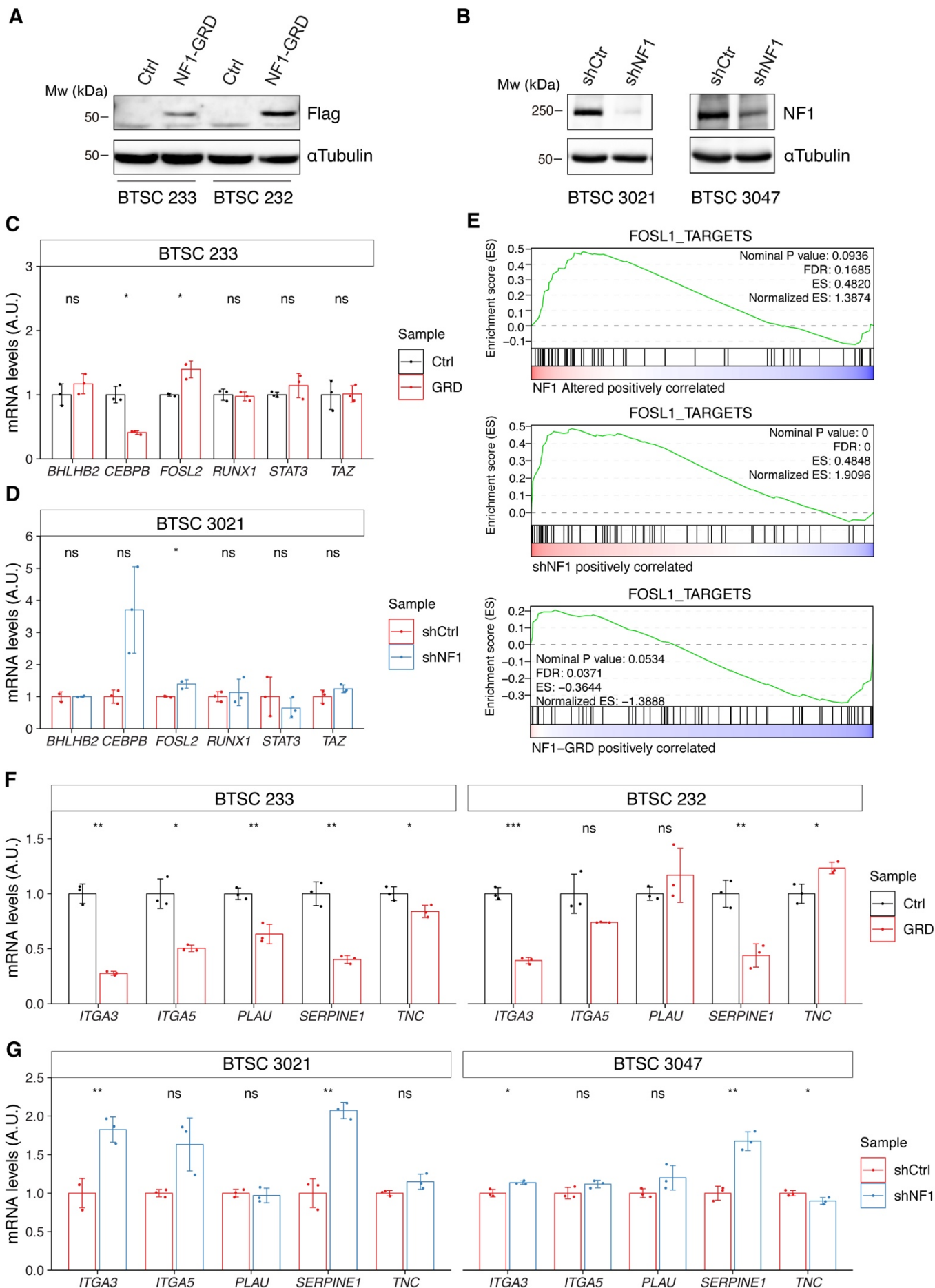


Figure S3. Related to Figure 2. **A)** Western blot analysis of FLAG-NF1-GRD expression in MES cells (BTSC 233 and 232). **B)** Western blot analysis of NF1 expression upon *NF1* knockdown in PN cells (BTSC 3021 and 3047). **C)** and **D)** qRT-PCR analysis of mesenchymal genes master regulators expression (*BHLHB2*, *CEBPB*, *FOSL2*, *RUNX1*, *STAT3* and *TAZ*) upon NF1-GRD overexpression in BTSC 233 (C) or *NF1* knockdown in 3021 cells (D). Data are presented as mean \pm SD (n=3), normalized to GAPDH or 18s rRNA expression; Student's t test, ns = not significant, *P \leq 0.05. **E)** GSEA of *FOSL1* targets signature in GBMs with *NF1* alteration or wt status (*top panel*), BTSC 3021 cells transduced with sh*NF1* or shCtrl (*middle panel*), and BTSC 233 cells transduced with NF1-GRD or Ctrl vector (*bottom panel*). **F)** and **G)** qRT-PCR analysis of known mesenchymal *FOSL1* targets (*ITGA3*, *ITGA5*, *PLAU*, *SERPINE1* and *TNC*) in BTSC 233 and 232 cells transduced with NF1-GRD expressing lentivirus (F) and BTSC 3021 and 3047 cells transduced with sh*NF1* expressing lentivirus. Data are presented as mean \pm SD (n=3), normalized to 18s rRNA expression; Student's t test, ns = not significant, *P \leq 0.05, **P \leq 0.01, ***P \leq 0.001.

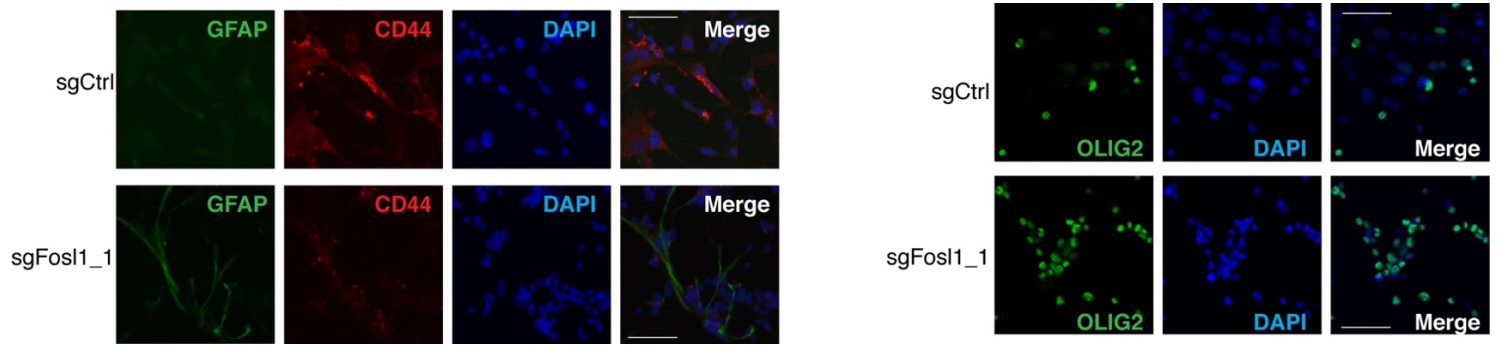


Figure S4. Related to Figure 4. Representative images of immunofluorescence staining of the indicated markers in sgCtrl and sgFosl1_1 p53-null *Kras*^{G12V} NSCs plated on laminin-coated coverslips. Scale bars represent 50 μ m.

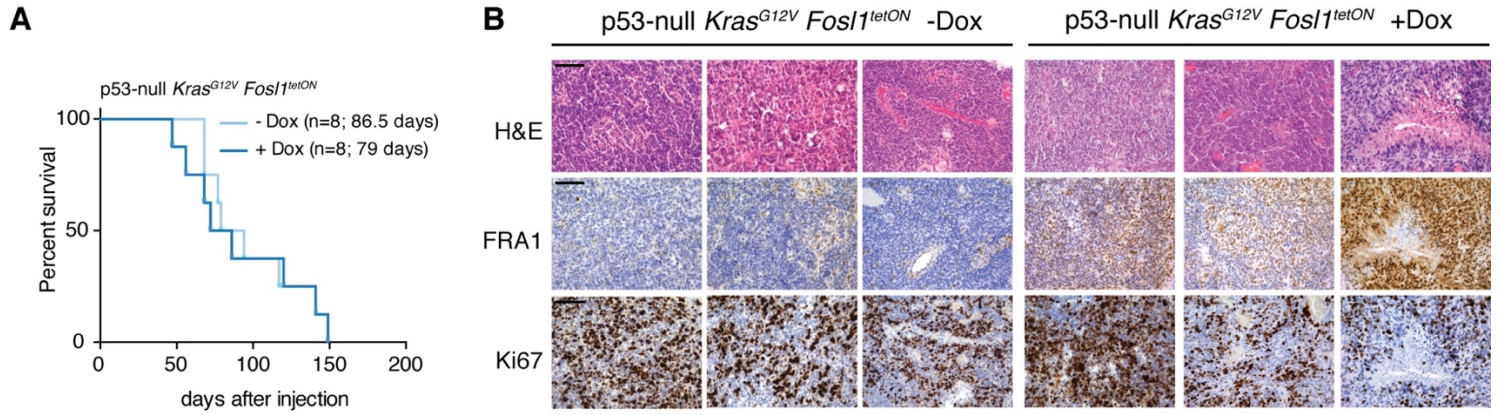


Figure S5. Related to Figure 5. **A)** Kaplan-Meier survival curves of C57BL/6J wildtype mice injected with p53-null *Kras*^{G12V} *Fosl1*^{tetON} NSCs subjected to Dox diet (n=8) or kept as controls (n=8); Log-rank P value = 0.814. **B)** Hematoxylin and eosin (H&E) and immunohistochemical staining, using the indicated antibodies, of representative -Dox and +Dox tumors. Scale bars represent 100 μ m.

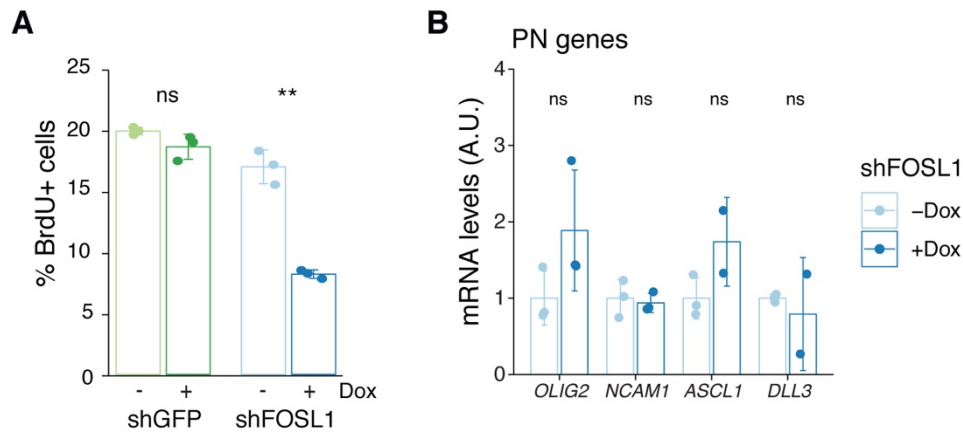


Figure S6. Related to Figure 6. A) BrdU incorporation of BTSC 349 shGFP and sh*FOSL1*, in absence or presence of Dox, analyzed by flow cytometry. Data from a representative of two independent experiments are presented as mean \pm SD (n=3). Student's t test, relative to the respective control (-Dox): ns = not significant, ** $P \leq 0.01$. **B)** mRNA expression of PN genes in BTSC 349 sh*FOSL1* in absence or presence of Dox for 3 days. Data from a representative of three experiments are presented as mean \pm SD (n=3), normalized to *GAPDH* expression. Student's t test, relative to -Dox: ns = not significant, * $P \leq 0.05$.